

DEPARTMENT OF PHYSICS AND ASTRONOMY  
UNIVERSITY OF HEIDELBERG

Monte Carlo Simulation  
of charmed meson reconstruction in the  
semi-leptonic decay channel  
 $D^{*+} \rightarrow D^0(K^- e^+ \nu_e)\pi^+$  at ALICE

BACHELOR THESIS IN PHYSICS

SUBMITTED BY

Georgijs Skorodumovs

BORN IN VENTSPILS (LATVIA)

2016



This Bachelor Thesis has been carried out by Georgijs Skorodumovs at the  
Physikalisches Institut, University of Heidelberg  
under the supervision of  
Priv.-Doz. Dr. Kai Schweda



# Abstract

Within this thesis a PYTHIA Monte-Carlo simulation was developed, in order to study the decays and reconstruction capabilities of  $D^*(2010)^+$  in semi-leptonic channel at midrapidity  $|y| \leq 0.5$  in the range  $0 \leq p_t \leq 30$  GeV/c at ALICE. The distributions of the reconstructed invariant masses  $M_0$  and  $M_*$  of  $D^0$ ,  $D^*$  mesons, as well as their difference  $\Delta M$  were studied, under the consideration of kinematic selections and ITS+TPC transverse momentum resolution. The  $\Delta M$  reconstruction method predicts the invariant mass distribution to appear as a sharp peak at the kinematic threshold, given by the pion mass, with a width of  $23$  MeV/c<sup>2</sup>. It was shown that the  $\Delta M$  distribution is insignificantly altered in the concerned momentum range if momentum resolution is regarded in the MC routine. Analysis of the detection efficiency predicts good reconstruction capabilities ( $\epsilon > 20\%$ ) of  $D^*$ -mesons with the transverse momenta  $p_{t,D^{*+};m.b.} > 4$  GeV/c,  $p_{t,D^{*+};TRD} > 8$  GeV/c. The total number of reconstructed  $D^*$  mesons (in the luminosity  $\mathcal{L}_{int} = 0.404 \mu\text{b}^{-1}$ ) is predicted to be  $N_{D^*} = 132.9_{-0.51}^{+0.79}$ , where the upper and lower uncertainties are given by the FONLL calculations of the prompt charm hadron production and feed-down correction. No signal has been seen in the analyzed raw data of p-Pb collisions at  $\sqrt{s} = 5.023$  TeV/c from the year 2013. Further improvements must be made.

# Zusammenfassung

Im Rahmen dieser Arbeit wurde eine PYTHIA Monte-Carlo Simulation entwickelt, um die Zerfälle und die Rekonstruktion von  $D^*(2010)^+$  in den semi-leptonischen Zerfallskanal bei Midrapidität  $|y| \leq 0.5$  im Intervall des transversalen Impulses  $0 \leq p_t \leq 30$  GeV/c mit ALICE zu analysieren. Es wurden die Verteilungen der invarianten Massen, sowohl  $M_0$  und  $M_*$  der  $D^0$ ,  $D^*$  Mesonen, als auch deren Differenz  $\Delta M$ , untersucht, indem die kinematischen Selektionen und die Auflösung des transversalen Impulses von ITS und TPC berücksichtigt wurden. An der kinematischen Grenze, die durch die Masse des positiven Pion entstand, lieferte die theoretische Rekonstruktion  $\Delta M$  einen 23 MeV/c<sup>2</sup> breiten Signal. Die Simulation hat gezeigt, dass der Einfluss der Impulsauflösung auf die Verbreitung der  $\Delta M$ -Verteilung geringfügig war. Die analysierte Detektionseffizienz  $\epsilon$  lässt eine gute Rekonstruktion der  $D^*$  Mesonen mit dem transversalen Impuls von  $p_{t,D^{*+};m.b.} > 4$  GeV/c,  $p_{t,D^{*+};TRD} > 8$  GeV/c voraussagen. Die Anzahl der rekonstruierten  $D^*$  Kandidaten wird der Wert  $N_{D^*} = 132.9_{-0.51}^{+0.79}$  erwartet, wo die integrierte Luminosität den Wert  $\mathcal{L}_{int} = 0.404 \mu\text{b}^{-1}$  beträgt, wobei die obere und die untere Messunsicherheiten durch FONLL-Rechnungen der Charm-Quark Produktion gegeben sind. In den analysierten Datenreihen der p-Pb Kollisionen bei  $\sqrt{s} = 5.02$  TeV/c aus dem Jahr 2013 wurde kein Signal gesehen. Weitere Verbesserungen sind notwendig.

# Contents

ABSTRACT	3
1 INTRODUCTION	8
2 CHARM QUARKS AND HADRONS AT LHC	11
2.1 Heavy quark production in pQCD	11
2.2 FONLL	14
2.3 Hadronization	15
2.4 Properties of open charm hadrons	16
3 CERN AND THE LHC EXPERIMENT	18
3.1 ALICE Detector System	19
3.2 Particle identification at ALICE	19
4 KINEMATICS OF DECAYS	26
4.1 Two body decay	26
4.2 Three-body decay	30
4.3 Decay angle	32
5 MONTE CARLO SIMULATION	34
5.1 Random number generators	34
5.2 Acceptance and rejection method (von Neumann)	38
5.3 Data simulation and collection	39
5.4 Identification of particles via PDG-code	39
5.5 Decay table	40
5.6 Defining the four-momentum components	41

5.7	Transverse momentum resolution . . . . .	41
5.8	MC decay routine . . . . .	43
5.9	Transverse momentum distributions . . . . .	45
5.10	Reconstruction of invariant masses . . . . .	48
5.11	Efficiency results . . . . .	58
6	NUMBER OF PARTICLES	60
6.1	Nuclear modification factor . . . . .	61
6.2	Luminosity at ALICE . . . . .	61
6.3	FONLL results . . . . .	62
6.4	Feed-down corrections . . . . .	63
6.5	Number of reconstructed particles . . . . .	64
7	DATA ANALYSIS	66
8	SUMMARY	70
	REFERENCES	73
	ACKNOWLEDGMENTS	76



# Listing of figures

1.1	The characteristic energy loss of bottom and charm quarks in QGP. Adronic, A. et al. (2016) . . . . .	9
1.2	The distributions of $\Delta\mathcal{M} = \mathcal{M}_* - \mathcal{M}_0$ in <i>left</i> : the hadronic (3-prong) decay channel $D^* \rightarrow D^0(K^- \pi^+) \pi^+$ and <i>right</i> : in the semi-leptonic decay channels $D^* \rightarrow D^0(K^- e^+ \nu_e) \pi^+$ and $D^* \rightarrow D^0(K^- \mu^+ \nu_\mu) \pi^+$ combined. The OPAL Collaboration (1997) . . . . .	10
2.1	Averaged relative abundance of charm quark fragmenting to hadrons, Lysovyi et al. (2015) . . . . .	16
3.1	Schematic view of the LHC experiments. . . . .	19
3.2	ALICE. ALICE collaboration (2014) . . . . .	20
5.1	An excerpt from the decay table file for the $D^{*+}$ meson . . . . .	40
5.2	The momentum resolution at ITS and TPC. . . . .	42
5.3	Transverse momentum distributions of positrons for different transverse momentum values of $D^*$ . The arrows indicate the kinematic thresholds. . .	46
5.4	Transverse momentum distributions of kaons for different transverse momentum values of $D^*$ . The arrows indicate the kinematic thresholds. . . .	46
5.5	Transverse momentum distributions of pions for different transverse momentum values of $D^*$ . The arrows indicate the kinematic thresholds. . . .	47
5.6	The reconstructed mass of $D^* \rightarrow D^0(K^- \pi^+) \pi^+$ without and with resolution	49
5.7	The reconstructed $\mathcal{M}_*$ without considering the momentum resolution . . .	51
5.8	The reconstructed $\mathcal{M}_*$ without considering the momentum resolution . . .	51

5.9	Invariant mass of $D^0$ as a function of $p_T$ . Pink line indicates mean value, shaded region corresponds to rms. The bars and circles(and small squares) indicitate the rms of $M_0$ distribution, when momentum resolution was taken into account . . . . .	52
5.10	Left: $M_0$ distribution for $p_T = 30$ of $D^*$ with considered momentum resolution. Right: positron transverse momentum vs. kaon transverse momentum. The magenta points on the right panel correspond to the magenta area on the left panel. . . . .	53
5.11	Invariant mass of $D^*$ as a function of $p_T$ . Pink line indicates mean value, shaded region corresponds to rms. The bars and circles(and small squares) indicitate the rms of $M_0$ distribution, when momentum resolution was taken into account . . . . .	54
5.12	The whole momentum of $D^0$ meson as function of the $D^*$ momentum. . .	54
5.13	The reconstructed $\mathcal{M}_*$ without resolution . . . . .	55
5.14	Invariant mass difference $\Delta M$ as a function of $p_T$ . Pink line indicates mean value, shaded region corresponds to rms. The bars and circles(and small squares) indicitate the rms of $M_0$ distribution, when momentum resolution was taken into account . . . . .	56
5.15	Geometrical acceptance, electron efficiency and total efficiency. On the left: the data has been analyzed in offline mode. On the right: the trigger on electrons has been applied . . . . .	58
5.16	Fraction of the total detection efficiency considering TRD trigger to the efficiency considering minimum bias trigger . . . . .	59
6.1	Left: Differential cross section of the prompt D hadron production calculated by the FONLL framework. Right: The differential cross section of $D^*$ production from bottom quarks. . . . .	62
6.2	The fraction of the prompt $D^*$ meson production to the total $D^*$ meson production . . . . .	64
7.1	The $\Delta M$ distribution. The analysis of the raw data. . . . .	68
7.2	The distributions of the decay angle of the pion from $D^* \rightarrow D^0$ . Left panel: the analysis of raw data. Right panel: MC simulation . . . . .	69

# 1

## Introduction

The main goal of ALICE (A Large Ion Collider Experiment) is the study of the properties of an exotic hadronic state of matter, called Quark Gluon Plasma (QGP), which is produced for a brief instant in heavy ion collisions under enormous temperature and pressure. Among the essential probes of QGP are the heavy charm and bottom quarks that are produced in heavy ion collisions due to their large mass.

The knowledge of both the production mechanisms and kinematics of heavy quarks can deepen our understanding of the important properties of QGP, such as transport properties and the energy loss of particles within the deconfined strongly interacting matter [Völkl \(2016\)](#). The type of interaction of charm and bottom quarks with the QGP depends on the energy they have. If the quarks carry large momenta, radiative processes occur, i.e. the quarks lose their energy via inelastic interactions when moving within the deconfined matter. Since the mass of the high-momentum quarks is negligible compared with their energy, the energy loss is no longer characteristic for each quark species and consequently bottom and charm quarks become indistinguishable in their interaction properties. Conversely low energy quarks show a specific behavior in QGP, which might depend on their mass. However, the transport properties of low-energy heavy quarks have not been experimentally studied

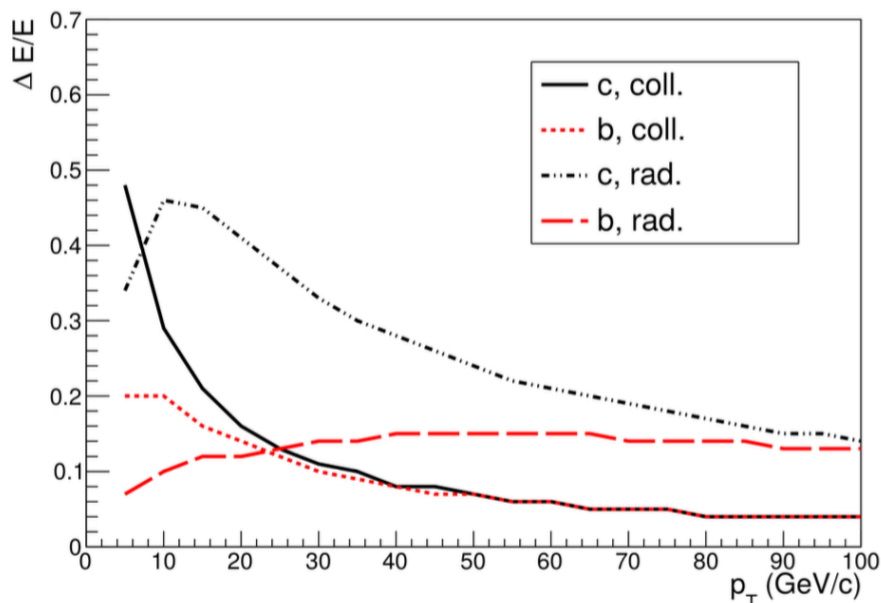


Figure 1.1: The characteristic energy loss of bottom and charm quarks in QGP. Adronic, A. et al. (2016)

yet. Nevertheless, there are theoretical predictions on the partonic energy loss in collisional and radiative processes both at low and large energy scales in Fig 1.1.

Since the heavy quarks hadronize into strong and weakly interacting heavy hadrons right after the production, no direct measurements can be done on heavy quarks within the QGP. Instead, an attempt is made at the identification of detectable daughter particles from decaying heavy hadrons. The collected kinematic and topological information from the identified candidates is then used to reconstruct the initial heavy-quark hadrons.

For instance, the heavy charm resonance  $D^*(2010)^+$  has a decay length of order of few pm and therefore it decays via the strong force long before it reaches the sensitive detector area. If it decays in the hadronic 3-prong channel  $D^*(2010)^+ \rightarrow D^0(K^-\pi^+)\pi^+$ , it is possible to reconstruct the parent D meson from the detectable charged particles. 3-prong decay is well studied at ALICE. However, the study of the semi-leptonic decays of the same D resonance is more challenging, since in the decay  $D^{*+} \rightarrow \pi^+K^-e^+ + \nu_e$ , the missing neutrino takes away a fraction of the momentum. Nevertheless, the goal of this thesis is to analyze and study the semi-leptonic decay channel of  $D^{*+}$ . There are at least several reasons for this.

First of all, the TRD trigger enables effective detection and identification of electrons and positrons, where TRD stands for the Transition Radiation Detector.

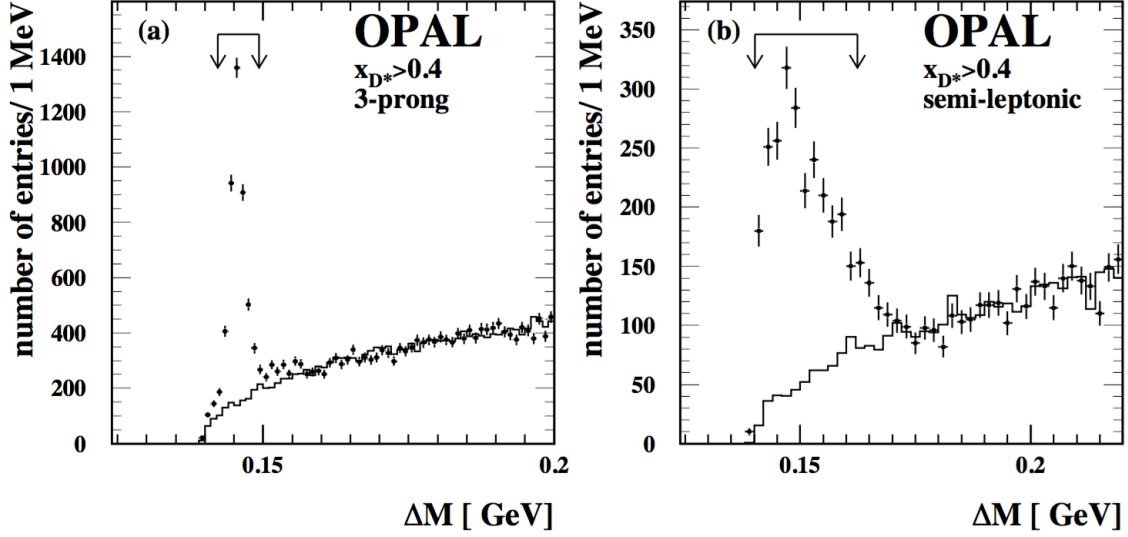


Figure 1.2: The distributions of  $\Delta M = M_* - M_0$  in left: the hadronic (3-prong) decay channel  $D^* \rightarrow D^0(K^- \pi^+) \pi^+$  and right: in the semi-leptonic decay channels  $D^* \rightarrow D^0(K^- e^+ \nu_e) \pi^+$  and  $D^* \rightarrow D^0(K^- \mu^+ \nu_\mu) \pi^+$  combined. The OPAL Collaboration (1997)

The reconstruction of  $D^*(2010)^+$  mesons from the semi-leptonic decay channel  $D^*(2010)^+ \rightarrow D^0(K^- e^+ \nu_e) \pi^+$  was inspired by the work of the OPAL collaboration, The OPAL Collaboration (1997) which proved that even in the case of the missing neutrinos, it is possible to reconstruct the mother  $D^*$ -resonance and obtain a very good signal to combinatorial background ratio by the application of a relatively simple method, see Fig.1.2. The extraction technique will be further referred to in this thesis as the  $\Delta M$ -method. This method involves the determination of the invariant masses of  $D^*$  and  $D^0$  candidates  $M_*$  and  $M_0$ , respectively, which are built from the reconstructed four-momenta of the charged daughter candidates  $K^-$ ,  $e^+$  and  $\pi^+$ .

Another source of motivation is the work done at CMS, which uses two types of jet discriminators to perform identification of displaced charm hadron jets, The CMS collaboration (2015). Each analyzed jet must have a very large transverse momentum  $p_t > 20$  GeV/c. This kinematic threshold hinders the possibility of analyzing the properties of low-momentum charm and bottom quarks. The techniques used at ALICE enable the particle identification and analysis even at very low transverse momenta. Accordingly, it is expected that low-momentum charm hadrons can be reconstructed, thus bridging a gap in the investigations of QGP.

# 2

## Charm quarks and hadrons at LHC

### 2.1 HEAVY QUARK PRODUCTION IN PQCD

When two projectile protons collide, their constituents, partons, interact with each other via the strong force. Because of the high energy scales, hard scatterings take place, i.e. gluons scatter and initial partons annihilate thus producing a wide diversity of particles, among them the charm quarks, [Moehler, C. \(2014\)](#).

Since the strong interaction conserves the quark flavour, the charm quarks are produced in charm-anticharm pairs ( $c\bar{c}$ ) via the scattering of either an initial quark-antiquark pair ( $q\bar{q}$ ) or two gluons  $g$ - $g$ .

The Leading Order (LO) processes are pair creation and quark annihilation, and Next-to-Leading Order (NLO) processes are gluon splitting and flavour excitation, [Völkl \(2016\)](#). The Order of an interaction is given by the number of vertices  $n$ , e.g.  $n = 2$  and  $n = 3$  relate to the LO and NLO processes, respectively. Each vertex (in turn) provides information about the interaction probability, which in the case of  $n$  vertices is  $\propto g_s^{2n} \propto \alpha_s^n$ . The dimensionless numbers  $g_s$  and  $\alpha_s$  stand for the interaction strength and the strong coupling constant, respectively.

The higher order interactions, such as Next-to-Next-to-Leading Order (NNLO) processes, also exist. However, at high energy scales their contributions to the cross section of the process are drastically suppressed and are mainly disregarded in perturbative quantum chromodynamics (pQCD) calculations.

In order to understand the mechanisms of charmonium production and hadronization, it is of utmost importance to know the properties of heavy quark production procedure. However, the cross sections of heavy quark production is not analytically calculable. One can make use of perturbative quantum chromodynamics (pQCD) for this purpose, Skands, P.Z. (2015). The differential cross section  $d\sigma$  can be expanded into a series in terms of the strong coupling constant  $\alpha_s$

$$d\sigma = \sum_{n=0}^{\infty} d\sigma^{(n)} \cdot \alpha_s^n \quad (2.1)$$

In comparison with the coupling constant of quantum electrodynamics (QED)  $\alpha_e \approx \frac{1}{137}$ , the strong coupling constant  $\alpha_s$  of QCD is dependent upon the energy scale  $Q^2$ . The coupling constant is usually given at some reference scale  $Q^2 = M^2$ , so that the value of  $\alpha_s$  can be determined at any other scale via

$$\alpha_s(Q^2) = \alpha_s(M^2) \frac{1}{1 + b\alpha_s(M^2) \ln(\frac{Q^2}{M^2}) + O(\alpha_s^2)} \approx \frac{1}{b \cdot \ln(\frac{Q^2}{\Lambda^2})}, \quad (2.2)$$

where  $b$  denotes a constant and  $\Lambda \approx 200 \text{ MeV}$  denotes the Landau pole. One can easily notice that, as  $Q \rightarrow \Lambda$  the strong coupling increases drastically  $\alpha_s \gg 1$ . This behavior of  $\alpha_s$  at low energy scales makes it impossible to apply QCD perturbative calculations to systems of any energy. By contrast, as  $Q \gg 200 \text{ MeV}$ , the coupling vanishes. This effect is called asymptotic freedom and implies that pQCD can be applied for systems of high energies.

One can write the formula for the fixed order differential cross section of heavy quark  $Q$  production in a hard scattering as

$$d\sigma^{FO} = \sum_{ij} \int dx_1 dx_2 F_1(x_1, \mu_F) F_2(x_2, \mu_F) d\sigma_{ij \rightarrow QX}(\alpha_s, x_1, x_2, \mu_F, \mu_R). \quad (2.3)$$

Eq.2.3 describes a situation where two light partons  $i$  and  $j$ , constituents of colliding particles, carry a fraction  $x_1$  and  $x_2$  of initial momentum of the particles, respectively, and interact with each other at very small distances, i.e.  $\alpha_s \ll 1$ .  $F_1$  and  $F_2$  are the parton distribution functions (PDFs), which can be viewed mathematically as probability density functions. The PDFs

show how probable it is for a certain parton  $i(j)$  to carry a fraction  $x_1(x_2)$  of the particle's momentum. The differential cross section  $d\sigma_{ij \rightarrow QX}$  encapsulates the information about the production probability of a heavy quark during the hard interaction of the partons  $i$  and  $j$ . The variables  $\mu_F$  and  $\mu_R$  are called factorization and resummation scales, respectively. These scales are chosen so as to minimize the uncertainties in pQCD calculations, and are set to  $\mu_{R,F} = \sqrt{m^2 + \hat{p}_t^2}$ , where  $m$  denotes the heavy quark mass. The differential cross section  $d\sigma(pp \rightarrow D + X)^{FO}$  is estimated via NLO calculations, i.e. up to the order  $O(\alpha_s^3)$ , [Mangano, Michelangelo L. et al. \(1992\)](#).

Eq.2.3 does not give a sufficient result if one wants to describe hadronization process that happens at relatively large distances, i.e. the coupling constant of strong interaction is bigger than unity(one) and pQCD methods cannot be applied. Moreover, NLO calculations yield unreliable results for the large momentum  $p_t$  values. For this reason, fragmentation functions (FF) are introduced. One can also speak of a factorization process. The differential cross section is then estimated as

$$d\sigma^{RS} = \sum_{i,j,k} \int dx_1 dx_2 dz F_1(x_1, \mu_F) F_2(x_2, \mu_F) d\sigma_{ij \rightarrow QX}(\alpha_s, x_1, x_2, \mu_F) \cdot D_c^{H_c}(z) \quad (2.4)$$

This time the summation goes not only over the light quarks, which are assumed to be massless, but also includes heavy quarks. The mass of the heavy charm quark  $m_c$  is neglected in Eq.2.4, as the calculation focuses on large momentum scales, i.e.  $p_t \gg m_c$ .  $D_c^{H_c}(z)$  is the fragmentation function (FF) and is viewed as the production probability density function of the hadron  $H_c$  possessing a fraction  $z$  of the four-momentum of the initial charm quark. It should be noted that FFs are not an object of pQCD calculations. The upper index  $RS$  in Eq.2.4 denotes the resummation to all orders including leading-logarithmic terms (LL) and next-to-leading-logarithmic terms (NLL) of the form  $\alpha_s(\alpha_s \log(\frac{p_t}{m}))^n$  and  $\alpha_s^2(\alpha_s \log(\frac{p_t}{m}))^n$ , respectively.

## 2.2 FONLL

FONLL, which stands for Fixed-Order plus Next-To-Leading Logarithmic resummation, is a framework that calculates the differential cross sections of heavy quark (both charm and bottom quarks) production within pp or p-Pb collisions, [Cacciari, M. et al. \(1998\)](#). The selections for the calculation can be done over transverse momentum  $p_t$  and either rapidity  $y$  or pseudorapidity  $\eta$ . The differential cross section  $d\sigma^{\text{FONLL}}$  is then estimated via

$$d\sigma^{\text{FONLL}} = d\sigma^{\text{FO}} + G(m, p_t) \cdot (d\sigma^{\text{RS}} - d\sigma^{\text{FOMo}}) \quad (2.5)$$

Consequently, FONLL combines the calculations at fixed order up to NLO with the resummation to all orders up to the NLL. Since some of the terms are included both in FO and RS calculations, the differential cross section  $d\sigma^{\text{FOMo}}$  is then subtracted from  $d\sigma^{\text{RS}}$ . Since the resummation neglects the mass of heavy quark, it has also be neglected in the FO calculation, this implies that  $d\sigma^{\text{FOMo}}$  is simply a massless limit of  $d\sigma^{\text{FO}}$ , i.e.  $d\sigma^{\text{FOMo}} = d\sigma^{\text{FO}}(p_t, \frac{m}{p_t} \rightarrow 0)$ . However, such a massless limit leads to inaccurate results as the transverse momentum gets very small, i.e  $p_t \leq am$ . To deal with this, the so-called suppression factor  $G(m, p_t)$  has been introduced and is given by

$$G(m, p_t) = \frac{p_t^2}{p_t^2 + a^2 m^2}. \quad (2.6)$$

The constant  $a$  is estimated to be equal to  $a = 5$ .

In this work the momentum and rapidity ranges have been set to  $p_t \in [0.5; 30.5]$  and  $y \in [-0.5, 0.5]$ , respectively. The value  $p_{t,\text{min}}$  was not set to zero, as the code yields unreliable results. The differential cross section  $\frac{d\sigma}{dp_t}$  was calculated within those kinematic selections for a pp collision at  $\sqrt{s} = 13 \text{TeV}$ .

## FONLL uncertainties

The uncertainties of FONLL calculations arise from uncertainties of mass, scales and PDF estimation.

Since the invariant masses of the quarks cannot be determined precisely, as the quarks are color confined, the values have been chosen to be  $m_c = 1.5 \pm 0.2 \text{ GeV}/c^2$  and  $m_b = 4.75 \pm 0.25 \text{ GeV}/c^2$  for charm and bottom quarks, respectively. If one varies these mass values within their uncertainties and keep all other parameters in FONLL calculations fixed at their central values, one gets the upper and lower mass uncertainty bands, i.e.  $d\sigma_{m,\text{MAX}}$  and  $d\sigma_{m,\text{MIN}}$ ,

respectively. The standard deviations are then calculated for each of the bands via

$$\Delta\sigma_{m,MAX(MIN)} = |d\sigma - d\sigma_{m,MAX(MIN)}|, \quad (2.7)$$

where  $d\sigma$  denotes the central value of the differential FONLL cross section. The lower index  $m$  denotes the dependence on mass.

The scales  $\mu_F$  and  $\mu_R$  are also varied about a central value, determined as  $\mu_R = \mu_F = \mu = \sqrt{\hat{p}_t^2 + m^2}$ , where  $m$  stands for the central value of the heavy quark mass, e.g.  $m_c = 1.5\text{GeV}$ . Hereafter we define  $\xi_F = \frac{\mu_F}{\mu}$  and  $\xi_R = \frac{\mu_R}{\mu}$ . The variation of the scales follows some constraints on the values of  $\xi_F$  and  $\xi_R$ , i.e. the following relations must hold:  $0.5 \leq \xi_F, \xi_R \leq 2$  and  $0.5 \leq \frac{\xi_R}{\xi_F} \leq 2$ . The calculations yield the upper and the lower bands scale uncertainty. The errors are calculated analogous to Eq.2.7:

$$\Delta\sigma_{scale,MAX(MIN)} = |d\sigma - d\sigma_{scale,MAX(MIN)}|. \quad (2.8)$$

Parton distribution functions cannot be evaluated using the pQCD techniques and therefore they also contribute to the uncertainty of results obtained with FONLL framework. The variation routine is discussed in [Cakir, H. \(2013\)](#). The default PDF setting of FONLL has been chosen to be CTEQ6.6. The envelope of uncertainty bands yield the errors

$$\Delta\sigma_{PDF,MAX(MIN)} = |d\sigma - d\sigma_{PDF,MAX(MIN)}|. \quad (2.9)$$

The total uncertainty of the estimated differential cross section is calculated as a quadratic sum of the corresponding errors from Eq.2.7-2.9.

### 2.3 HADRONIZATION

The produced  $c\bar{c}$  pair is a high energy resonance which is unstable and therefore decays in separated charm and anticharm quarks. Since the quarks cannot exist independently, they must recombine with other quarks, thus unifying into various baryons and mesons. If one charm quark hadronizes with one or several lighter quarks (u,d,s), then one speaks of open-charm hadrons.

However, particles are not created with equal probability in the fragmentation process. At this point the fragmentation fractions will be briefly introduced.

A fragmentation fraction  $f(q \rightarrow H_q)$  represents a probability of the quark  $q$  to hadronize

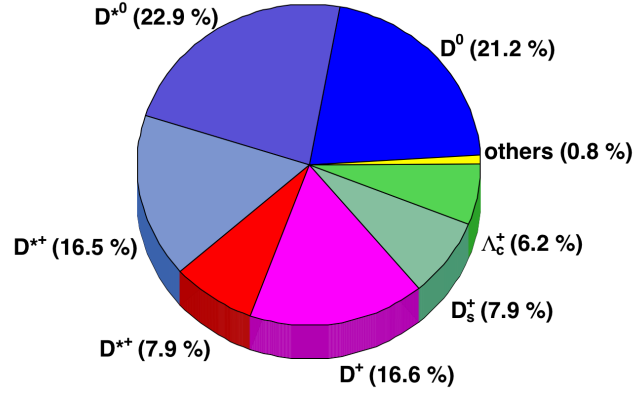


Figure 2.1: Averaged relative abundance of charm quark fragmenting to hadrons, Lysovyi et al. (2015)

into a certain hadron  $H_q$ . The sum over all possible fragmentation fractions for a given quark (here, charm) is equal to unity. The fragmentation is considered to be invariant under the production process. Fig.(2.1) depicts the charm fragmentation fractions averaged over data collected in  $e^\pm p$ ,  $e^+ e^-$  and  $pp$  collisions. The hadronization is assumed to take place in vacuo.

The  $D^*(2007)^0$  resonance decays fully ( $BR = 100\%$ ) to  $D^0$  mesons; the  $D^*(2010)^+$  decays with unequal branching ratios both to  $D^0$  and  $D^+$  mesons. The summation over percentage values of blue pie slices yields a value of the total fragmentation fraction  $f(c \rightarrow D^0)$ . The sum of the values from the red and magenta pie slices determines the whole fragmentation fraction contributing to  $D^+$  production. One can see that in collisions the  $D^0$  mesons are produced more copiously than other open charm mesons.

#### 2.4 PROPERTIES OF OPEN CHARM HADRONS

The produced D mesons are not stable. Their natural decay length  $c\tau$  is calculated as

$$c\tau = \frac{\hbar c}{\Gamma}, \quad (2.10)$$

where  $c$ ,  $\hbar$  and  $\Gamma$  denote the speed of light, the Dirac constant and the full decay width, respectively. The Tables below contain some information about the D mesons, including their quark content, mass, natural decay width, as well as the most important decay channels and their branching ratio.

Meson	quark content	mass (MeV/c <sup>2</sup> )	$c\tau$ (pm)	decay channel	$B_i$ (%)
$D^*(2010)^+$	$c\bar{d}$	$2010.3 \pm 0.1$	$\sim 30$	$D^0\pi^+$ $D^+\pi^0$ $D^+\gamma$	$\sim 68$ $\sim 30$ $< 2$

**Table 2.1:** Properties of  $D^*(2010)^+$  meson. The values are taken from Olive, K.A. et al. (2014)

Meson	quark content	mass (MeV/c <sup>2</sup> )	$c\tau$ ( $\mu m$ )	decay channel	$B_i$ (%)
$D^0$	$c\bar{u}$	$1864.8 \pm 0.1$	120	$K^- e^+ \nu_e$	$\sim 3.6$
				$K^- \pi^+$	$\sim 3.9$
$D^+$	$c\bar{d}$	$1869.6 \pm 0.1$	310	$K^- 2\pi^+$	$\approx 9.1$

**Table 2.2:** Properties of  $D^0$  and  $D^+$  mesons. The values are taken from Olive, K.A. et al. (2014)

# 3

## CERN and the LHC experiment

The main goal of CERN (European Organization for Nuclear Research) is to explore the fundamental particles, their interactions and properties. For this purpose the Large Hadron Collider, or LHC, is being run at CERN. The LHC is the most powerful particle accelerator ever built in the world. It operates at the highest energy scales, e.g. the center-of-mass energy in pp collisions has reached up to  $\sqrt{s} = 13$  TeV, and delivers the highest collision luminosities ever seen in the lab.

There are four main particle detectors that serve at LHC, named ALICE (A Large Ion Collider Experiment), ATLAS (A Toroidal LHC Apparatus), CMS (the Compact Muon Solenoid) and LHCb (LHC beauty). Their schematic positions in LHC can be seen in Fig. (3.1).

The aims of the ATLAS experiment are the exploration of the properties of the Higgs Boson, as well as the investigation of physics beyond the standard model, for instance, evidence of supersymmetry. The physics program of CMS pursues the similar goal as those of ATLAS, including the research of heavy ion collisions. The decays of hadrons, containing bottom or charm quarks, are the main subject matter of the LHCb experiment, which also specializes in precision tests of CP Violation. ALICE studies the properties of the quark-gluon plasma

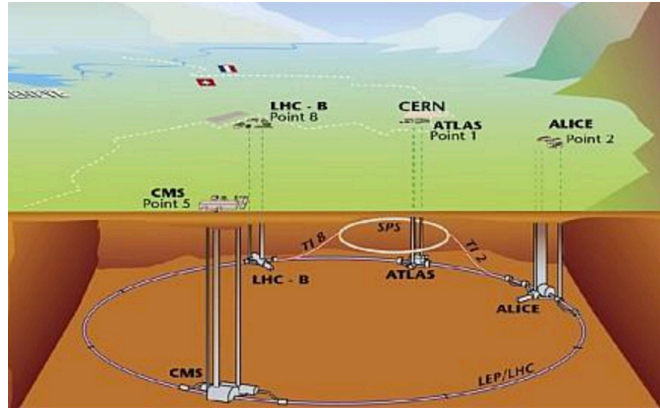


Figure 3.1: Schematic view of the LHC experiments.

(QGP), an exotic, strongly interacting state of matter that forms under very high matter densities and temperatures.

### 3.1 ALICE DETECTOR SYSTEM

The objective of ALICE is to deepen understanding of properties of QGP, which is formed for a brief instant in head-on lead-lead, proton-proton or proton-lead collisions, [ALICE collaboration \(2014\)](#). ALICE provides both track measurements and reconstruction of particles in a wide momentum interval from 100 MeV/c to 100 GeV/c. The central sub-detectors cover the pseudorapidity region  $|\eta| < 0.9$  and are surrounded by the L<sub>3</sub>-magnet, which produces a homogeneous magnetic field of about  $B = 0.5$  T in the direction of the beam axis. The main barrel tracking detectors at ALICE are Inner Tracking System (ITS), Time of Flight Chamber (TOF), Transition Radiation Detector (TRD) and Time of Flight (TOF) detector. These detectors are able to collect information about particles in the mid-momentum range. ALICE also provides measurements of muons, photons and cosmic rays. The functional principles of the main barrel detectors will be further discussed.

### 3.2 PARTICLE IDENTIFICATION AT ALICE

The 7 out of 16 detectors exploited at ALICE can provide particle identification (PID). Each of the central barrel detectors with full azimuthal coverage, employs a unique PID-technique in a specific particle momentum range. The combination of detectors makes PID possible over a broad momentum interval, reaching up to  $p_T = 100$  GeV/c. However, since most of the produced daughter particles possess low momenta, the emphasis is made on the PID in

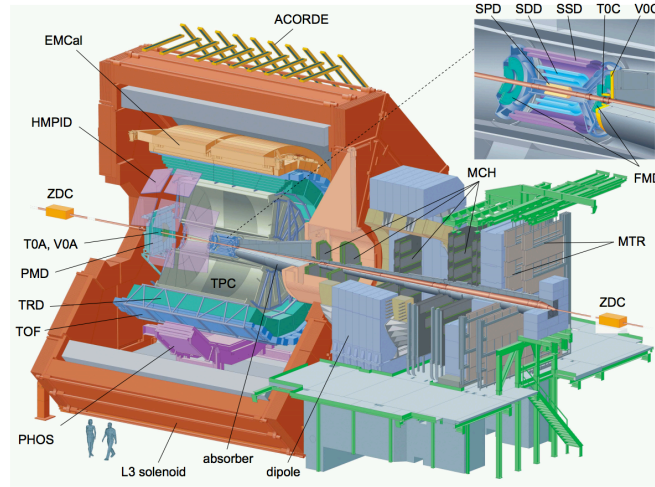


Figure 3.2: ALICE. ALICE collaboration (2014)

the small momentum range. Further the performance of the main central barrel detectors will be briefly discussed.

**Inner Tracking System** The Inner Tracking System (ITS) is a cylindrical detector situated close to the beam axis. The body of ITS consists of six silicon layers, whose radial distance to the beam axis lies between 3.9 and 43.0 cm. The main goal of ITS is to precisely reconstruct the position of the primary interaction vertices and secondary vertices of decaying heavy hadrons, such as D-mesons, with a resolution of about  $100 \mu\text{m}$ . ALICE collaboration (2010). Moreover, ITS enables both the track reconstruction and identification of charged particles at low transverse momentum  $p_T < 200 \text{ MeV}$  and enhances the tracking performance of the Time Projection Chamber (TPC).

**Time Projection Chamber** The acronym TPC stands for the Time Projection Chamber, which is adapted both to measure the trajectories of charged particles in three-dimensional space and to reconstruct particle jets in ultrarelativistic heavy ion collisions, making use of their characteristic energy loss when moving through material, Lippmann (2012). The mean energy loss  $\langle \frac{dE}{dx} \rangle$  of particles with  $0 \leq \gamma\beta \leq 1000$  crossing certain media is well described by the

Bethe-Bloch equation, [Patrignani \(2016\)](#):

$$-\left\langle \frac{dE}{dx} \right\rangle = Kz^2 \frac{Z}{A} \frac{1}{\beta^2} \left( \frac{1}{2} \ln \frac{2m_e c^2 \beta^2 \gamma^2 T_{max}}{I^2} - \beta^2 - \frac{\delta(\beta\gamma)}{2} \right), \quad (3.1)$$

as  $z$  and  $Z$  denote the charge of the crossing particle and the atomic number of absorber, respectively;  $A$  is the atomic mass of the absorber,  $m_e$  denotes electron mass,  $T_{max}$  the maximum energy deposit to the free electron of the medium in a collision,  $I$  stands for the ionization constant, characteristic for each material;  $\delta(\beta\gamma)$  describes the correction factor for the energy loss within ionization. One notices that the energy loss given by Eq.3.1 does not depend on the particle mass, thus being dependent only on the factor  $\beta$  and the properties of the absorber. This property of Bethe-Bloch equation can be used for the PID. The measured mean energy loss, which is commonly lower than predicted by Eq.3.1, can be plotted against the measured particle momentum.

As can be seen, the PID capabilities are strongest at low momenta. Kaons and pions can be identified and separated from each other, as they carry kinematic momentum lower than 700 MeV/c. The overlapping of uncertainty bands at  $p \geq 1$  GeV/c makes the separation almost impossible. TPC does not manage to identify high-momentum electrons ( $p_t \geq 3$  GeV/c) precisely, as the energy loss is suppressed by a factor of 100 and makes electrons and pions indistinguishable.

If the transverse momentum of the charged particle is large, the effects of multiple scattering can be neglected. Charged particles are bent in a magnetic field  $B \approx 0.5T$ . The bending radius  $R$  can be estimated using the following equation:

$$p_t = 0.3BR \left[ \frac{GeV}{T \cdot m} \right]. \quad (3.2)$$

In order to determine the uncertainty of the momentum, one measures the sagitta  $s$  of the track, i.e. the geometric distance between the center of a certain arc and the centre of its base, [Niebuhr \(2007\)](#). If one considers the central angle  $\Theta$  to be very small, as the radius  $R$  is very large compared to the distance  $L$  between the first track and the last detected track  $N$ , it can be approximated as

$$\frac{L/2}{R} = \sin \frac{\Theta}{2} \approx \frac{\Theta}{2}, \quad (3.3)$$

and therefore

$$\Theta \approx \frac{L}{R} \quad (3.4)$$

Using this approximation one can easily estimate the value of the sagitta

$$s = R\left(1 - \cos\frac{\Theta}{2}\right) \approx R\frac{\Theta^2}{8} = \frac{0.3 BL^2}{8 p_t} \quad (3.5)$$

The relative momentum uncertainty is supposed to depend only on the uncertainties of the sagitta measurement, and therefore

$$\frac{\sigma_{p_t}}{p_t} = \frac{\sigma_s}{s} = \frac{8p_t}{0.3BL^2}\sigma_s, \quad (3.6)$$

as the uncertainty  $\sigma_s$  is considered to be constant and is dependent principally on the position resolution in the transverse plane  $\sigma_{xy}$

$$\sigma_s = \sqrt{\frac{720}{N+4}}\sigma_{xy} \quad (3.7)$$

where the factor  $\sqrt{720}$  is given by Gluckstern, [Gluckstern \(1963\)](#), and  $N$  denotes the number of equidistant track measurements. Combining the results from Eq.3.6. and 3.7. one notices the relation

$$\frac{\sigma_{p_t}}{p_t} = ap_t \quad (3.8)$$

as  $a$  is a constant. The result in Eg. 3.8 implies that the resolution of momentum measurements worsens with the increasing transverse momentum of particles. This might be explained due to the increasing bending radius, which in turn reduces the value of the sagitta and thus degrades its estimation possibility.

When a certain particle carries low momentum and crosses the surface of detectors, it scatters at both the atoms of the material and gas molecules. This statistical process is called multiple scattering (MS), [Patrignani \(2016\)](#). This effect causes a deflection of the initial particle's track and thus makes a contribution to determination of spatial resolution and consequently to the momentum resolution. One can show than the contribution from the MS is given by the relation, [Niebuhr \(2007\)](#)

$$\left(\frac{\sigma_{p_t}}{p_t}\right)^{MS} = \frac{0.2}{\beta B\sqrt{LX_0}\sin\Theta} = \frac{b}{p\sqrt{\sin\Theta}}, \quad (3.9)$$

where  $\beta$  describes the velocity of the crossing particle,  $p$  denotes the momentum of the particle;  $B$  and  $L$  are the values of the magnetic field and the transverse length, respectively.  $X_0$

stands for the radiation length. The angle  $\Theta$  represents the angle between the momentum direction and the beam axis, i.e.  $p_t = p \cdot \sin\Theta$ . One sees that for particles with  $p_z = 0$  the contributions from MS yield the minimum of the trajectory deviation. As the value of  $\Theta$  gets smaller, particles penetrate through a larger volume of the detecting material. This leads to an increase in the momentum uncertainty. The limit  $\Theta \rightarrow 0$  results in the singularity of the resolution function and does not have any physical interpretation for the produced particles within collisions, as particles with  $p_t = 0$  are not detected.

Combining the contributions from hit resolution, Eq.3.8., and those of MS, Eq.3.9, one simply gets

$$\frac{\sigma_{p_t}}{p_t} = ap_t \oplus \frac{b}{p\sqrt{\sin\Theta}} \quad (3.10)$$

i.e. the uncertainties are added in quadrature.

### Transition Radiation Detector

The primary target of the Transition Radiation Detector (TRD) is to identify high-energy electrons, [Lippmann \(2006\)](#). Its functional principle is based on the detection of characteristic transition radiation, emitted by electrons (positrons) that possess a transverse momentum larger than 1 GeV/c. Penetration of particles with high transverse momenta ( $\gamma \geq 1000$ ) through the interface between two media with unequal dielectric constants leads to the emission of photons with energy

$$E \approx \frac{1}{4} \hbar \omega_p \gamma, \quad (3.11)$$

where

$$\omega_p = \sqrt{\frac{n_e e^2}{\epsilon_0 m_e}}, \quad (3.12)$$

$\omega_p$  stands for plasma frequency,  $e$  the value of the unit electron charge,  $\epsilon_0$  is the dielectric constant in vacuo, and  $n_e$  and  $m_e$  are electron density and mass, respectively, [Dolgoshein \(1993\)](#).

TRD serves not only to enhance the momentum resolution for detectable particles with high values of  $p_T$ , but also to acquire a rapid trigger for energetic charged particles.

A huge number of particles being produced in a single high energy collision leads to a enormous amount of data, which is collected by the Data Acquisition (DAQ) system, [Anticic, T. et al. \(2005\)](#). For instance, in Pb-Pb collisions at  $\sqrt{s_{NN}} = 5.02$  TeV data rates can exceed the value of 25 GB/s, which surpasses the capabilities of DAQ which has typical data rates of 1 GB/s. The implemented trigger system helps not only to reduce the amount of acquired

data, but also to filter rare events (with probability per collision  $\leq 10^{-5}$ ), Klein (2011), which might contain physics information and help to study the properties of the QGP.

The main goals of the TRD trigger is the enhancement of high-momentum electrons, setting the kinematic threshold to  $p_t \geq 3$  GeV/c; and separation of electrons from pions, which can be performed by using the information of reconstructed tracks and characteristic properties of transition radiation for both particles.

The presence of the trigger makes it more probable to detect  $D^{*+}$  mesons which decay in semi-leptonic channel rather than those that decay in any other channels.

### Time Of Flight detector

Charged particles possessing intermediate values of momentum, typically 0.5 - 4 GeV/c, can be identified with help from TOF, which stands for Time-Of-Flight detector, Akindinov (2010). TOF makes use of Multigap Resistive Plate Chambers (MRPC), Sun, Y.I. et al. (2008). The main part of MRPC is a collection of resistive glass plates, which are positioned parallel and very close to each other. The space between two contiguous plates is filled with non-flammable gas mixture. Cathode pickup electrodes build up the outer part of the chamber, at which a high voltage is applied. The operation philosophy of MRPC lies in the production and subsequent readout of electron avalanches as charged particles ionize the gas in the gaps between resistive glass plates. MRPCs provide very precise measurements of time of flight of charged particle.

The particle identification technique is based on the measurement of particle charge and its mass. Since the mass cannot be measured straightforwardly, at least two independent measurements of kinematic quantities that include information about the mass have to be performed at the same time. For this reason, both time of flight  $t$  and the absolute value of the 3-momentum  $p$  are measured by TOF, Preghenella (2009). The velocity is calculated as  $v = L/t$ , as  $L$  is a fixed length of flight, which is equal to  $L=3.7$  m. The mass of the particle is calculated via the relativistic momentum-energy relation:

$$m^2 = \frac{p^2}{c^2} \left( \frac{c^2 t^2}{L^2} - 1 \right), \quad (3.13)$$

where  $c$  denotes the speed of light in vacuo. In order to distinguish between two particles having different masses  $m_1$  and  $m_2$ , one compare their values of time of flight  $t_1$  and  $t_2$ , as they

possess the same value of momentum  $p$ . Using the time resolution of TOF,  $\delta t = 80$  ns, the number of standard deviations  $n_\sigma$  is calculated via

$$n_\sigma = \frac{t_1 - t_2}{\delta t} = \frac{Lc}{2p^2\delta t}(m_1^2 - m_2^2). \quad (3.14)$$

One can immediately notice that the identification performance worsens with increasing momentum of particles. For example, kaons and pions, with a mass difference of  $m_K - m_\pi \approx 350$  MeV/c<sup>2</sup> are viewed as not distinguishable ( $n_\sigma < 3$ ), if their momentum exceeds the value of ca.  $p = 2.5$  GeV/c. Pions and electrons,  $m_\pi - m_e \approx m_\pi \leq 140$  MeV/c, can be separated, if the momentum is lower than 700 MeV/c.

# 4

## Kinematics of decays

This section is dedicated to calculation of maximum and minimum values of transverse momenta of daughter particles  $K^-$ ,  $e^+$  and  $\pi^+$ . Consequently the results obtained in MC simulations will be checked for adequacy, as compared with theoretical predictions.

The values for invariant masses of the particles are taken from the decay table, see Sect.2.4,

### 4.1 TWO BODY DECAY

In this section the kinematics of two-body decays will be discussed using the example of  $D^*(2010)^+ \rightarrow D^0\pi^+$ . To begin with, the momentum of the daughter particles will be calculated in the rest frame of the mother  $D^*$  resonance. It will be followed by the estimation of the minimum and maximum values of transverse momentum of the slow pion in the case when the mother particle carries a fixed value of the momentum perpendicular to the initial beam axis  $p_T$  and is boosted in the z-direction at rapidity range  $|\gamma| \leq 0.5$ .

Let the  $D^*$  meson decay in the rest frame; its mass will be denoted as  $M$  throughout the discussion. Furthermore, let the energies and momenta of  $D^0$  and  $\pi^+$  be given as  $E_D$  and  $E_\pi$ ,  $\vec{p}_D$  and  $\vec{p}_\pi$ , respectively. The four-momenta  $P$ ,  $P_D$  and  $P_\pi$  correspond to  $D^*$ ,  $D^0$  and  $\pi^+$ ,

respectively. Due to 3-momentum conservation the daughter particles are emitted back to back in the rest frame, i.e.

$$\vec{p}_\pi = -\vec{p}_D := \vec{p}. \quad (4.1)$$

Moreover, one can easily find the relation  $P \cdot P_\pi = ME_\pi$ , and therefore

$$m_D^2 = P_D^2 = (P - P_\pi)^2 = m_\pi^2 + M^2 - 2ME_\pi. \quad (4.2)$$

Extrapolating  $E_\pi$  out of the eq.(4.2), using the relativistic energy-momentum relation and setting the values for corresponding masses, one can estimate the absolute value of the 3-momentum

$$|\vec{p}| = \sqrt{E_\pi^2 - m_\pi^2} = \frac{1}{2M} \sqrt{[(M - m_\pi)^2 - m_D^2] \cdot [(M + m_\pi)^2 - m_D^2]} \approx 38.4 \text{ MeV}/c \quad (4.3)$$

Now it is assumed that the daughter particle possesses a transverse momentum  $p_T$  in the laboratory frame and decays in the same channel as above. Assigning  $p_T > 0$  to  $D^*$  can also be mathematically viewed as boosting the particle from its rest frame in  $p_T$  direction by a certain Lorentz factor  $\gamma_T$ . In the considered case one should mention the relativistic equation

$$\vec{p}_T = \vec{\beta}_T \gamma_T M = \vec{\beta}_T E, \quad (4.4)$$

where  $\vec{p}_T$ ,  $M$  and  $E$  denote transverse momentum, mass and energy of a  $D^{*+}$ , respectively.

It is convenient to represent the system in the cylindrical coordinates. Since one is interested only in the value of the transverse momentum of the daughter particles and not in its direction, it is straightforward to simplify this such that the direction of the momentum  $\vec{p}_{T,\pi}$  coincides with the x-Axis and the angle between  $\vec{p}_{T,\pi}$  and  $\vec{p}_T$  will be denoted by  $\phi$ , with

$0 \leq \phi \leq 2\pi$ . The boost Lorentz matrix  $\Lambda$  in the x-y plane is then given by

$$\begin{aligned} \Lambda_{x-y,\phi} &= \begin{pmatrix} \gamma & \beta_x \gamma & \beta_y \gamma & 0 \\ \beta_x \gamma & 1 + (\gamma - 1) \frac{\beta_x^2}{\beta^2} & (\gamma - 1) \frac{\beta_x \beta_y}{\beta^2} & 0 \\ \beta_y \gamma & (\gamma - 1) \frac{\beta_x \beta_y}{\beta^2} & 1 + (\gamma - 1) \frac{\beta_y^2}{\beta^2} & 0 \\ 0 & 0 & 0 & 1 \end{pmatrix} \\ &= \begin{pmatrix} \gamma_T & \beta_T \gamma_T \cos(\phi) & \beta_T \gamma_T \sin(\phi) & 0 \\ \beta_T \gamma_T \cos(\phi) & 1 + (\gamma_T - 1) \cos^2(\phi) & (\gamma_T - 1) \sin(\phi) \cos(\phi) & 0 \\ \beta_T \gamma_T \sin(\phi) & (\gamma_T - 1) \sin(\phi) \cos(\phi) & 1 + (\gamma_T - 1) \sin^2(\phi) & 0 \\ 0 & 0 & 0 & 1 \end{pmatrix} \quad (4.5) \end{aligned}$$

Let  $P_T$ ,  $P_{D,T}$  and  $P_{\pi,T}$  denote the four-momenta of the particles analog to the notation above. In the new frame,

$$P_T = P_{D,T} + P_{\pi,T}. \quad (4.6)$$

On the other hand, taking into account the assumptions discussed above one can write

$$P_T = \Lambda_{x-y,\phi} \cdot P = \Lambda_{x-y,\phi} (P_D + P_\pi). \quad (4.7)$$

Identifying the new momentum of the pion  $P_{\pi,T}$  with the expression  $\Lambda_{x-y,\phi} P_\pi$  yields

$$P_{\pi,T} = \Lambda_{x-y,\phi} \begin{pmatrix} E_\pi \\ p_{T,\pi} \\ 0 \\ p_z \end{pmatrix} = \begin{pmatrix} \gamma_T E_\pi + \beta_T \gamma_T \cos(\phi) p_{T,\pi} \\ \beta_T \gamma_T \cos(\phi) E_\pi + (1 + (\gamma_T - 1) \cos^2(\phi)) p_{T,\pi} \\ \beta_T \gamma_T \sin(\phi) E_\pi + (\gamma_T - 1) \cos(\phi) \sin(\phi) p_{T,\pi} \\ p_z \end{pmatrix} \quad (4.8)$$

The squared magnitude of the transverse momentum  $p_{T,\pi,\gamma_T}$  of the  $\pi^+$  meson is then equal to

$$p_{T,\pi,\gamma_T}^2(\phi, p_{T,\pi}) = ((\gamma_T^2 - 1) \cos^2(\phi) + 1) p_{T,\pi}^2 + 2\beta_T \gamma_T^2 E_\pi p_{T,\pi} \cos(\phi) + (\gamma_T \beta_T E_\pi)^2 \quad (4.9)$$

Finding the extremum values of the expression in eq.(4.9) automatically yields the extremum values for  $p_{T,\pi,\gamma_T}$ . One might also notice that the values of  $p_{T,\pi}$  are in the range  $0 \leq p_{T,\pi} \leq p$ , where  $p$  was calculated in eq. (4.3). The z-component of the 3-momentum remains unchanged after boosting in the transverse plane and does not contribute to the value given in eq.(4.9). It can be proved that the function shown in eq.(4.9) does not have any local ex-

trema inside the open set of domain  $(D_{p_{T,\pi}} \times D_\phi)_{open} = (0, 2\pi) \times (0, p)$ . Since this function is continuous and is defined over compact set, its extrema are found on the boundaries of the domain.

The maximum of the presented function is given at the point  $\mathcal{A}(\phi, p_{T,\pi}) = (0, p)$ , i.e. the value of the transverse momentum of the emitted particle must be equal to the absolute value of its kinematic momentum and coincide with the direction of the boost. It can be explicitly written

$$p_{T,\pi,\gamma_T,MAX} = \gamma_T \beta_T E_\pi + \gamma_T p, \quad (4.10)$$

with  $E_\pi = \sqrt{m_\pi^2 + p^2}$ . In order to find the minimum value, one estimates the partial derivative of the observed function with respect to the variable  $\phi$  and finds out, that the particle has to be emitted in the opposite direction of transverse boost, i.e.  $\phi = \pi$ . Consequently it can be simply shown that the transverse momentum to be determined is given by

$$p_{T,\pi,\gamma_T,MIN} = \gamma_T \beta_T E_\pi - \gamma_T p \quad (4.11)$$

Finally, the mother particle is then boosted in z-direction in rapidity range  $|y| \leq 0.5$ . The rapidity  $y$  can be mathematically defined as the angle of a hyperbolic rotation, i.e. of the Lorentz transformation between two reference frames, and is given as

$$y = \frac{1}{2} \ln \left( \frac{E + p_z}{E - p_z} \right), \quad (4.12)$$

where  $v$  stands for the velocity of the relative motion and  $c$  is defined as the speed of light. The Lorentz matrix  $\Lambda_z$  can be explicitly given as:

$$\Lambda_z = \begin{pmatrix} \gamma & 0 & 0 & \gamma\beta \\ 0 & 1 & 0 & 0 \\ 0 & 0 & 1 & 0 \\ \gamma\beta & 0 & 0 & \gamma \end{pmatrix} = \begin{pmatrix} \cosh(y) & 0 & 0 & \sinh(y) \\ 0 & 1 & 0 & 0 \\ 0 & 0 & 1 & 0 \\ \sinh(y) & 0 & 0 & \cosh(y) \end{pmatrix} \quad (4.13)$$

Using similar considerations as above and eq.(4.6) and eq.(4.7), one can write down an

expression for the z- and  $p_T$ -boosted four-momentum of pion  $P_{\pi,z-T}$ :

$$P_{\pi,z-T} = \Lambda_z \Lambda_{x-y,\phi} P_\pi = \begin{pmatrix} E_{\pi,\gamma_T} \cosh(\gamma) + p_z \sinh(\gamma) \\ \vec{p}_{T,\pi,\gamma_T} \\ E_{\pi,\gamma_T} \sinh(\gamma) + p_z \cosh(\gamma) \end{pmatrix}, \quad (4.14)$$

where  $E_{\pi,\gamma_T}$  denotes the energy given in the last term of eq.(4.8). One notices immediately that boosting in z-direction does not have any impact on the value of transverse momentum. Moreover, it is noticeable that the Lorentz boost matrices  $\Lambda_z$  and  $\Lambda_{x-y,\phi}$  commute

$$\Lambda_z \Lambda_{x-y,\phi} = \Lambda_{x-y,\phi} \Lambda_z, \quad (4.15)$$

which can be proven e.g. by a simple matrix multiplication.

## 4.2 THREE-BODY DECAY

The kinematics of three-body decays will be further discussed using the example of  $D^0 \rightarrow K^- e^+ \nu_e$ . The case of the decay of one particle into three daughter particles is in general mathematically more complex and difficult to handle. It is impossible to precisely calculate the kinematic properties (energy and momentum) independently for each particle, since energy and momentum conservation, as the only conditions, make the kinematics of each particle in 3-body decay dependent on the kinematics of the other two particles. However, it is possible to estimate both minimum and maximum values of the momenta, considering some simple assumptions. This section is focused on the calculation of transverse momenta ranges for detectable daughter  $K^-$  and  $e^+$ . The obtained values will be used as a kinematic test in the Sect.5.7.

Let assume that the mother  $D^*(2010)^+$  resonance decays in its rest frame via the decay channel  $D^*(2010)^+ \rightarrow D^0 \pi^+$ . As was shown in Section 4.1, the daughter D-meson has a constant momentum equal to  $|p| = 0.038 \text{ GeV}/c$ . The decay of the daughter  $D^0$  can be considered in its rest frame, for simplicity in the further calculations. Consequently, the four-momenta of  $D^0$ ,  $K^-$  and  $e^+$  will be denoted as  $P_D = (M_D, \vec{0})$ ,  $P_K = (E_K, \vec{p}_K)$  and  $P_e = (E_e, \vec{p}_e)$ , respectively. The four-momentum of the electron-neutrino  $P_\nu$  will not be explicitly given.

In order to determine the possible maximum transverse momentum of kaons and positrons it will be assumed that the electron-neutrino carries negligibly little energy, thus leaving a

larger phase space to the charged daughter particles. The approximation  $P_\nu \approx 0$  reduces the 3-body decay to a more simple 2-body decay, discussed in previous section, and therefore it will be regarded in the further calculations. The absolute value of the 3-momentum of both  $K^-$  and  $e^+$  in the rest frame of  $D^0$  can be then evaluated using the Eq.4.3. If one neglects the mass of the positron  $m_e$ , which is approximately only 0.1% of the kaon mass  $m_k$ , one can simply calculate

$$p_{K/e} = |\vec{p}_K| = |\vec{p}_e| \approx \frac{M_D^2 - m_k^2}{2M_D} = 0.867 \text{ GeV}/c. \quad (4.16)$$

The maximum transverse momentum is equal to the value in Eq. 4.16, i.e.  $p_{t,max} = p_{K/e}$ . In order to move to the rest frame of  $D^{*+}$ , one should boost  $D^0$ , analogous to the discussion in Section 4.1. Assume that the transverse momentum of  $D^0$ -meson  $p_{t,D}$  has its maximum and shows in the direction of  $p_{t,max}$ . These considerations for  $D^0$  kinematics lead to the estimation of the maximum transverse momentum of kaons (positrons). The decay of  $D^0$  in the rest frame of the mother particle can be then given by

$$P_{D,p_{t,D}} = \Lambda_{p_{t,D}} P_D \approx \Lambda_{p_{t,D}} (P_K + P_e) = \Lambda_{p_{t,D}} P_K + \Lambda_{p_{t,D}} P_e \quad (4.17)$$

i.e. the boost can be applied on the daughter kaons and positrons individually. The maximum of the transverse momentum of e.g. kaon  $p_{t,K}$  will be estimated using Eq.4.4 and 4.10 and relativistic momentum-energy relation

$$p_{t,K} = \frac{p}{M_D} E_k + \frac{\sqrt{(M_D^2 + p^2)}}{M_D} p_{K/e} \quad (4.18)$$

Using Eq.4.18 one can also easily find the relation between the maximum transverse momentum of positrons  $p_{t,e}$  and that of kaons  $p_{t,K}$

$$p_{t,e} = \frac{p}{M_D} (E_e - E_k) + p_{t,K} \quad (4.19)$$

As the relation holds  $E_e^2 = m_e^2 + p_{K/e}^2$  and  $E_K^2 = m_K^2 + p_{K/e}^2$ . One can notice from Eq.4.19 that due to the small mass daughter positrons carry less energy than daughter kaons, i.e.  $E_e < E_k$ , and therefore reach smaller momentum ranges.

In order to view the system in the laboratory frame one should also boost the initial parent  $D^{*+}$  meson. Using the considerations discussed in the previous section one determines the

maximum value of the transverse momentum  $p_{t,K,MAX}$  and  $p_{t,e,MAX}$  of kaons and positrons, respectively:

$$p_{t,K,MAX} = \gamma_T \beta_T E_{t,K} + \gamma_T p_{t,K} \quad (4.20)$$

and

$$p_{t,e,MAX} = \gamma_T \beta_T E_{t,e} + \gamma_T p_{t,e}, \quad (4.21)$$

where  $E_{t,e}^2 = m_e^2 + p_{t,e}^2$ . The energy  $E_{t,K}$  is determined analogously.

If the energy of the emitted neutrinos is taken into account, momentum conservation allows both kaons and positrons to have no transverse component of the momentum, i.e.  $p_t = 0$ .

### 4.3 DECAY ANGLE

Decay angle is defined as the angle  $\Theta^*$  between the momentum direction of the emitted daughter particle and the flight direction of the mother particle, according to the rest frame of the mother particle.

Since the kinematic quantities of daughter particles produced by virtual decays within PYTHIA are given in the laboratory frame, the calculation will be presented, which is dedicated to the determination of the decay angle.

Let's assume that the four-momentum of mother particle of mass  $M$  and daughter particle are given as  $P_m = (E_m, \vec{p}_m)$  and  $P_d = (E_d, \vec{p}_d)$ , respectively. Moreover, let's define the parallel component  $p_{||}$  of the daughter 3-momentum, as the projection of on the 3-momentum of mother particle

$$p_{||} = \frac{\vec{p}_m \cdot \vec{p}_d}{|\vec{p}_m|}, \quad (4.22)$$

and the perpendicular momentum  $p_{\perp}$  of the daughter particle (orthogonal to the flight direction of the parent particle) as

$$p_{\perp} = \sqrt{p_d^2 - p_{||}^2} \quad (4.23)$$

Furthermore, let's rotate the coordinate system around the interaction (decay) point in a way, so that the new instant z-direction coincides with the flight direction of the parent particle. In the next step let's apply a Lorentz matrix on the system, in order to go to the rest frame of the parent particle. The form of the matrix is given in Eq.4.13. The parameters are  $\gamma = E_m/M$  and  $\gamma\beta = -p_m/M$ . Due to the linearity of the vector space, the Lorentz transformation

matrix can be applied on each four-momentum independently. The Lorentz boost alters only the value of  $p_{||}$  and does not change the transverse component  $p_{\perp}$ . The new value  $p_{||,r.f.}$  in the rest frame of the mother particle(r.f.) is given as

$$p_{||,r.f.} = \gamma p_{||} + \gamma\beta E_d = \frac{E_m p_{||} - E_d p_m}{M} \quad (4.24)$$

The absolute value of the 3-momentum of daughter particle in r.f. is simply  $p = \sqrt{p_{||,r.f.}^2 + p_{\perp}^2}$ . The cosine function of the decay angle is the calculated as

$$\cos\Theta^* = \frac{p_{||,r.f.}}{p} \quad (4.25)$$

With the help of the ROOT class TLorentzvector all of the components of the momenta, as well as values of the energy in the laboratory frame can be collected.

# 5

## Monte Carlo Simulation

A Monte-Carlo (MC) simulation is used, in order to predict the behavior of the systems which cannot be calculated analytically, e.g. a probability distribution of physical quantities of the daughter particle stemming from a 3-body decay. The MC techniques base on the randomness of the happening events and therefore make use of the pseudorandom number generators, which not only produce uniformly distributed number sequences, but also help sampling distribution density functions. The following sections make a briefly overview of the pseudorandom number generators (PNRG) and acceptance-rejection method von Neumann.

### 5.1 RANDOM NUMBER GENERATORS

The MC-simulation method studied in this thesis makes use of the pseudo-random number generators (PRNG), i.e. numerical algorithms that enable the generation of numbers, which almost fulfill the properties of sequences of random numbers. PRNGs are basically deterministic generators and that implies that the produced sequences of numbers are not random.

The generation of the number sequence starts with an initial value, so called "seed", which is denoted as  $x_0$  in the following. Each next produced number depends on the previous one. The correlation between two next-standing numbers  $x_n$  and  $x_{n+1}$  in the PRN sequence can be expressed by a certain mathematical relation. This results in a reproducibility of the sequence, i.e. if the  $x_0$  is fixed at a certain value, the produced number sequences will be the same, as the same PRNG is run any number of times.

Another property of PRNG is its period, which denotes the least number  $L \geq 0$ , for which holds  $x_L = x_0$  and for each next element of the sequence one can find the relation  $x_n = x_{n+L}$ , as  $0 \leq n \leq L$ . Of course, one demands the period of PRNG to be very large, in order to get more accurate statistical results. However, the presence of a period is one of the PRNG drawbacks, since it depends on the chosen value  $x_0$  and the sequence cannot be infinitely long.

One of the important advantage of the PRNG is its speed of the random number generation, at modern computers it takes less than a second, in order to produce  $10^8$  32-digit numbers.

Furthermore, to the other important properties which a PRNG must fulfill count :

- 1) the generated numbers must be uniformly distributed
- 2) the next-bit-unpredictability must be ensured, in order to provide e.g. a high level cryptographic security.
- 3) PRNG has to be portable, i.e. the generation of the sequence does not depend on the system, by which it might be performed
- 4) PRN generators ought to require minimum memory on the system.

There is a huge variety of the developed PRNGs. For instance, the Blum-Blum Schub (B.B.S) PNRG produces a number sequence, in which the relation holds [Blum et al. \(1982\)](#)

$$x_{n+1} = x_n^2 \bmod M \quad (5.1)$$

as  $M = pq$  is a product of two usually large primes. The seed  $x_0$  can be any number, which is co-prime to  $M$ . The periodicity depends on the chosen prime numbers  $p$  and  $q$ , as well as on the seed. In the following sections two main PRNGs, which are implemented in ROOT

software, are discussed.

#### LINEAR CONGRUENTIAL GENERATOR

Another example of PRNG is a linear congruential generator (LCG). James, F. (1990) This generator is the best known and deeply studied PRNG. It has not only a historical importance, but is also implemented in the ROOT class *TRandom*. The generated sequence within LCG obeys a rather simple recurrence relation

$$x_{n+1} = (ax_n + c) \bmod m \quad (5.2)$$

as  $m > 0$  denotes the modulus, a positive integer  $a < m$  is called a multiplier, a non-negative integer  $c < m$  stands for increment. As the multiplier is set to the value  $a = 22695477$  and the increment is  $c = 1$ , the value of modulus  $m$  represent a very large number  $m = 2^{31} \approx 10^9$ , which in turn defines the periodicity of the LCG. One should not use the LCG, if the statistical processes are studied, since LCG shows an auto-correlation in the generation of low order numbers. Another drawback of LCG, is its relatively slow speed compared to other PRNGs. For these reasons, LCG was not implemented into the decay routine.

#### MERSENNE TWISTER

The PRNG, used in this work to collect good statistics of the virtual particle decays, is called Mersenne Twister, Matsumoto & Nishimura (1998). This PRNG is implemented into the ROOT class *TRandom3* and its generation principle is rather more complex than that of LCG. Mersenne Twister algorithm makes use of the following recurrence relation

$$x_{n+k} = x_{k+m} \oplus (x_k^u | x_{k+1}^l) \mathcal{A} \quad (5.3)$$

as  $x$  are called *word vectors* and are elements of the  $\nu$ -dimensional elements of the vector space  $\mathbb{F}_2^\nu$ , as  $\mathbb{F}_2 = \{0, 1\}$  denotes the binary number field. The constant transformation matrix is denoted by  $\mathcal{A}$ , which is an element of  $\mathbb{F}_2^{\nu \times \nu}$ . The indexes in Eq.5.3 are set as follows. The degree of the recurrence is denoted by the integer  $n > 0$ , the constant integer  $m$  is found in the interval  $1 \leq m \leq n$ , the integer  $k$  obeys the inequality  $k \geq 0$ . The integers  $n$ ,  $m$  and  $r$  are the constants of Mersenne Twister.

The generation of sequence starts with initializing of the first  $n$  seeds  $x_0, x_1 \dots x_{n-1}$ , as the  $k = 0$ . The word vector  $x_n$  is then obtained with the help of the recurrence relation. Then

one sets the integer values to  $k = 1, 2, \dots$ , in order to generate  $x_{n+1}, x_{n+2}, \dots$ . The word vector  $x_k^u$  stands for the  $r$  first *upper* bits of  $x_k$ , i.e. if  $x_k = (x_{k,\nu-1}, \dots, x_{k,0})$ , then  $x_k^u = (x_{k,\nu-1}, \dots, x_{k,r})$  with the condition  $0 \leq r \leq \nu - 1$ . The word vector  $x_{k+1}^l$  is given by the *lower*  $r$  bits of  $x_{k+1}$ , i.e.  $x_{k+1}^l = (x_{k+1,r-1}, \dots, x_{k+1,0})$ . The word vector  $(x_k^u | x_{k+1}^l)$  is calculated as the concatenation of the word vectors  $x_k^u$  and  $x_{k+1}^l$  in the corresponding order, i.e.  $(x_k^u | x_{k+1}^l) = (x_{k,\nu-1}, \dots, x_{k,r}, x_{k+1,r-1}, \dots, x_{k+1,0})$ .

The matrix  $A$  is chosen in a way, to guarantee a fast number generation. The rational normal form of  $A$  is

$$A = \begin{pmatrix} 0 & I_{\nu-1} \\ a_{\nu-1} & (a_{\nu-2}, \dots, a_0) \end{pmatrix} \quad (5.4)$$

as  $I_{\nu-1}$  denotes the identity matrix of the dimension  $(\nu - 1) \times (\nu - 1)$ , the word vector  $a = (a_{\nu-1}, a_{\nu-2}, \dots, a_0)$  is a constant. The form of the matrix  $A$  enables to simplify the multiplication operation. One can easily find the relation

$$(x_k^u | x_{k+1}^l) A = \text{shiftright}((x_k^u | x_{k+1}^l)) \oplus (a \cdot x_{k+1,0}), \quad (5.5)$$

as the function *shiftright* replaces the  $k-1$ -component of the word vector by its  $k$ -component, if the notation as above is used. The first component  $x_{k,\nu-1}$  is replaced by 0. Each component of  $a$  is multiplied by the value  $x_{k+1,0}$  and then the vectors are binary added up (the sign  $\oplus$  denotes the bitwise summation modulo two). The generated integer  $x_{n+k}$  is then gained by the bitwise addition of  $x_{n+m}$  and the word vector in Eq.5.5.

The word vectors, which represent pseudorandom integers, are given in the decimal number system as

$$(x)_2 = \left( \sum_{n=0}^{\nu} x_n \cdot 2^n \right)_{10} \quad (5.6)$$

as the lower indexes correspond to the type of the number system and  $x_n$  are the components of the word vector. The produced integers are considered to be uniform distributed and are generated in the range from 0 to  $2^\nu - 1$ . The output numbers are then obtained by the division of the integers by  $2^\nu - 1$ , which results in an uniform number distribution in the range  $[0, 1]$ . The period of the Mersenne Twister is given by the Mersenne prime  $2^{19937} - 1 \approx 10^{6000}$ , i.e.  $\nu = 19937$ , which ensures a generation of large sequences of uniform distributed numbers. One of the further advantage of this PRNG is its fast speed compared to LCG.

## 5.2 ACCEPTANCE AND REJECTION METHOD (VON NEUMANN)

The acceptance-rejection method is one of the Monte Carlo techniques and is used to generate a continuous distribution of variables  $f(x)$ , Casella, G et al. (2004). In order to apply this method, the properties of probability density distribution function  $f(x)$  must be known beforehand. Then one defines an envelope  $C \cdot b(x)$  that encloses  $f(x)$  completely, as  $C$  is a given constant and  $b(x)$  is a more simple density distribution function than  $f(x)$ . One must take into account, that both  $f(x)$  and  $b(x)$  are normalized to unity.

When a variable  $x$  is generated, the values of  $C \cdot b(x)$  and  $f(x)$  are computed. Then another independent value  $y$  is produced. If the relation

$$f(x) \geq yCb(x) \tag{5.7}$$

holds, then the variable  $x$  is *accepted*. Otherwise, it is rejected and the simulation starts from the beginning. For instance, if one chooses the uniform distribution  $b(x) = \mathbb{1}_{[a,b]}$  on a given interval  $[a, b]$ , then the envelope will be simply a rectangle of the width  $a - b$  and height  $C$ . If the analyzed distribution is a normalized Gaussian probability density function  $f(x) = G(\mu, \sigma; x)$ , then the optimal value of the height is  $C_0 = G(\mu, \sigma; x = \mu) = \frac{1}{\sigma\sqrt{2\pi}}$ . One should remind, that the value of  $C$  can be also be larger than  $C_0$ , however, it reduces the efficiency of simulation, which equals to the ratio of the areas, i.e.  $1/C$ . The acceptance and rejection method was used by W.Hörmann und G.Derflinger, Hoermann & Derflinger (1990), in order to develop a very fast technique for generation of normally distributed random variables, which is implemented into the function  $Gaus(\mu, \sigma)$  of the ROOT class  $TRandom$ . The function  $Gaus(\mu, \sigma)$  was used in this thesis to generate the normally distributed values of the central transverse momentum  $p_{T\gamma}$  in order to take the detector momentum resolution into account.

## 5.3 DATA SIMULATION AND COLLECTION

A specific Monte Carlo simulation was programmed in the modular software ROOT, in order to simulate the decays  $D^{*+} \rightarrow D^0(K^- e^+ \nu_e)\pi^+$  via PYTHIA and collect the statistical data that in turn was saved into large blocks of data, so-called '*trees*', both qualitatively and quantitatively analyzed and compared with real data. The main points of the simulation procedure will be explained in the sections below.

The number of trials, i.e. the number of decays of  $D^{*+}$  to happen, was set to  $N = 10^6$ , which yielded sufficient analyzable statistics while ensuring a suitable execution time.

## 5.4 IDENTIFICATION OF PARTICLES VIA PDG-CODE

The particles are specified via characteristic numbers, also known as PDG-codes, taken from the particle numbering scheme, [Garren et al. \(2016\)](#). This scheme, particularly implemented in PYTHIA, is used to encode relevant significant information about particles, such as the value of spin, quark content and internal quantum numbers, i.e. parity eigenvalues. PDG codes are positive 7-digit (integer) numbers of the form

$$\text{PDG-code} = \pm n n_r n_L n_{q_1} n_{q_2} n_{q_3} n_J \quad (5.8)$$

and are assigned to *particles*; the related *antiparticles* are given the negative value of the corresponding number. For instance, the pdg-code for  $D^*(2010)^+$  is equal to 413 = 0000413 and reveals the information that the particle does not belong to any exotic states such as excited gluons or quarks, technicolor states, pentaquarks states etc ( $n = 0$ ). It does not represent a radially excited state above the ground state ( $n_r = 0$ ) and the angular momentum of the system  $L$  is equal to zero ( $n_L = 0$ ). Moreover, this hadron is a meson ( $n_{q_1} = 0$ ) and is composed of one charm quark ( $n_{q_2} = 4$ ) and a down quark ( $n_{q_3} = 1$ ), as there is no differentiation between quarks and anti-quarks in this scheme. The total spin  $J = L + S$  of the meson is calculated via the last number, i.e.  $2J + 1 = 3$  and therefore  $J = 1$ . This information helps to conclude that the  $D^*(2010)^+$  meson is a *vector* meson, i.e.  $J^P = 1^-$ , where  $P$  denotes the parity eigenvalue. The *pseudoscalar* meson  $D^0$  with  $J^P = 0^-$  is given the number 421. The PDG codes for kaons  $K^-$ , positrons  $e^+$ , pions  $\pi^+$  and electron-neutrinos  $\nu_e$  are given by  $(-321)$ ,  $(-11)$ ,  $(211)$  and  $(12)$ , respectively.

```

413 D*+      D*-      3 0 1      2.01000      0.00000      0.00000      0.00000E+00 0 1
    1 3      0.683000      421      211      0      0      0
   -1 3      0.306000      411      111      0      0      0
   -1 0      0.011000      411      22      0      0      0

```

Figure 5.1: An excerpt from the decay table file for the  $D^{*+}$  meson

## 5.5 DECAY TABLE

The decay table stores information that agrees with the predictions of the Standard model. Fig.(5.1) depicts an excerpt of this table with the whole information about the decay possibilities of  $D^*(2010)^+$ . The table is constructed as follows.

In the first row one finds the basic physics parameters concerned with a particle. The first entry in the row is the PDG-code, discussed in the previous section. The next two entries show the symbols both of the particle and its anti-particle and are followed by the particle electric charge in units of  $\frac{|e|}{3}$ , where  $|e|$  denotes the elementary charge; the color-charge, or baryon number, which is equal to zero in the case of mesons. The number 1 afterwards confirms the presence of an anti-particle; otherwise 0 should be entered. The next term shows the value not encoded in pdg-codes - the invariant mass of the lifetime particle in units of  $\text{GeV}/c^2$ . Those values were explicitly used in the MC simulation. The next four zero-valued entries contain information about the lifetime and properties connected to the decay width. The last term defines whether the particle is assumed to be stable (0), or not (1).

The rows below include information about decay channels and their properties. The value of the first entry in each row can be set either to be equal to 1, if the certain decay channel exists, or to -1 otherwise. The following two entries depict the type of matrix element and the corresponding value of the branching ratio. The next five entries are filled with the PDG-codes of the daughter particles, where a distinction is made between particles and antiparticles.

Since only the decay channel concerned with  $D^*$  meson  $D^* \rightarrow D^0\pi^+$ , with a natural branching ratio  $BR(D^* \rightarrow D^0\pi^+) = 0.683$ , is studied in this work, the other possible decay channels  $D^* \rightarrow D^+\pi^0$  and  $D^* \rightarrow D^+\gamma$  were switched off, as shown in Fig.5.1. Analogously, in the case of decays of  $D^0$  meson, only the *electron* channel  $D^0 \rightarrow K^-e^+\nu_e$  was switched on. This procedure allows the branching ratio values to be altered, i.e. here, the branching ratios were set such that  $BR(D^* \rightarrow D^0\pi^+)_{MC} = BR(D^0 \rightarrow K^-e^+\nu_e)_{MC} = 1$ . The lower index *MC* stands for Monte Carlo simulation. Since the aim was to collect the kinematic information of the daughter particles ( $K^-$ ,  $e^+$  and  $\pi^+$ ), which in turn can decay, they were set to be *stable* in the simulation.

## 5.6 DEFINING THE FOUR-MOMENTUM COMPONENTS

In order to simulate the decay of a given mother particle, not only does it have to be initialized via its PDG-code and properties depicted in the decay table, but also its four-momentum  $P$  must be explicitly defined. The four-momentum was set to be dependent on the following three parameters: the mass of the initial decaying D-meson  $m_{D^*}$ , its transverse momentum  $p_T$  and its rapidity  $y$ . The last two parameters had to be simulated.

## TRANSVERSE MOMENTUM

The values of the transverse momentum of the initial  $D^*(2010)^+$  meson were uniformly distributed in a range from 0 GeV/c to 30 GeV/c, inclusively. The components  $p_x$  and  $p_y$  of the kinematic momentum were set as

$$p_x = p_y = \frac{1}{\sqrt{2}}p_T. \quad (5.9)$$

This simple assumption ( $p_x = p_y$ ) does not have any dramatic impact on the collected statistics, since the number of trials is large.

## RAPIDITY

In order to take into account the detector acceptance of the ALICE detectors, the values of mid-rapidity are obtained via flat distribution in a range from  $-0.5$  to  $0.5$ . The  $z$ -component of the kinematic momentum is calculated as

$$p_z = \sinh(y) \cdot \sqrt{m_{D^*}^2 + p_T^2}. \quad (5.10)$$

The energy  $E$  is then given explicitly by

$$E = \sqrt{m_{D^*}^2 + p_T^2 + p_z^2}. \quad (5.11)$$

## 5.7 TRANSVERSE MOMENTUM RESOLUTION

The uncertainties in the transverse momentum measurements using the ITS and TPC have been taken into account in this thesis. The Fig.5.2 depicts the relative momentum resolution  $\sigma_{p_t}/p_t$  as function of transverse momentum  $p_t$ . The plot was obtained from Monte Carlo simulation at CERN and checked against real data.

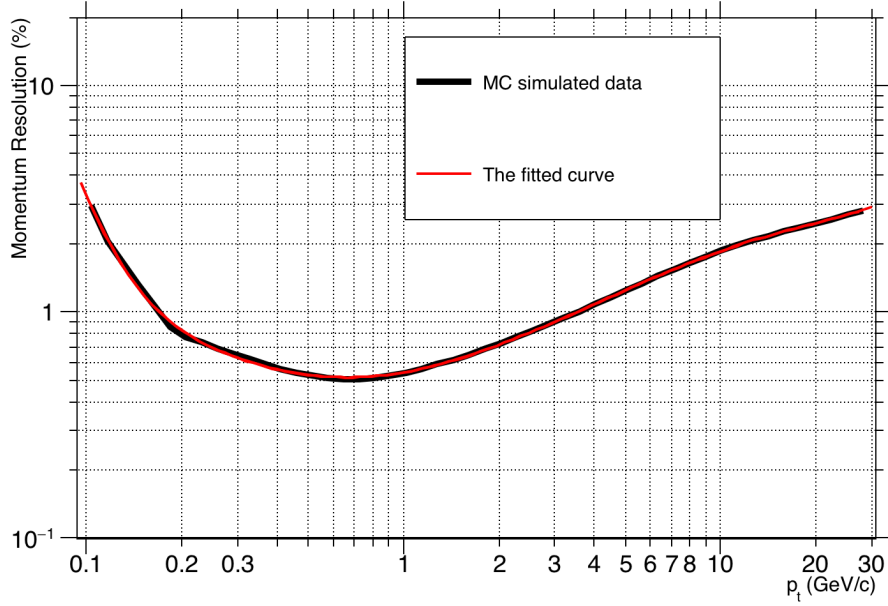


Figure 5.2: The momentum resolution at ITS and TPC.

The curve was fitted by a function  $f(p_t)$  which was assumed to be a polynomial with integer exponents of the form

$$f(p_t) = \sum_{n=-4}^4 a_n p_t^n, \quad (5.12)$$

and, for simplicity, dependent only on the values of transverse momentum. The negative exponents were included into the fitting function in order to consider the contributions of multiple scattering. The fitting momentum range was set to  $p_t \in [0.1, 30.0] \text{ GeV}/c$ . The coefficients  $a_n$  and their statistic uncertainties  $\Delta a_n$  are shown in the Table.??, a  $\chi^2$ -test yields  $\chi^2 \approx 0.01$ .

One sees that the particles with the lowest acceptable transverse momentum  $p_t \approx 100 \text{ MeV}/c$  and the largest transverse momentum  $p_t \approx 30 \text{ GeV}/c$  yield the largest uncertainties;  $\sigma_{p_t}/p_t \approx 4\%$  and  $\sigma_{p_t}/p_t \approx 2\%$ , respectively. The tracks of particles with  $0.5 \text{ GeV}/c \leq p_t \leq 1 \text{ GeV}/c$  are reconstructed very precisely with  $\sigma_{p_t}/p_t \approx 0.5\%$ .

The uncertainty of the  $p_t$  measurement was then calculated as

$$\sigma_{p_t} = 0.01 \cdot f(p_t) \cdot p_t, \quad (5.13)$$

where only the central values of coefficients  $a_n$  were used for the further MC-simulations, i.e.

n	$a_n$	$\Delta a_n$
-4	$4.04 \cdot 10^{-4}$	$1.18 \cdot 10^{-4}$
-3	$-2.64 \cdot 10^{-3}$	$2.41 \cdot 10^{-3}$
-2	$6.56 \cdot 10^{-3}$	$1.66 \cdot 10^{-2}$
-1	0.10	$4.52 \cdot 10^{-2}$
0	0.18	$4.58 \cdot 10^{-2}$
1	0.26	$1.55 \cdot 10^{-2}$
2	$-1.28 \cdot 10^{-2}$	$1.95 \cdot 10^{-3}$
3	$3.27 \cdot 10^{-4}$	$9.73 \cdot 10^{-5}$
4	$-3.11 \cdot 10^{-6}$	$1.64 \cdot 10^{-6}$

**Table 5.1:** The fitting parameters for the transverse momentum resolution function

no uncertainties  $\Delta a_n$  were taken into account.

In order to account for the resolution  $\sigma_{p_t}$ , the theoretical central value of transverse momentum  $p_t$  for each charged daughter particle (kaon, positron and pion), which was obtained within each single simulated decay of  $D^{*+}$ , had to be "interchanged" by a value  $\tilde{p}_t$  from a Gaussian distribution  $G(p_t; \mu = p_{t,central}, \sigma_t)$  with a mean at central  $p_t$  and the deviation equal to  $\sigma_{p_t}$  defined in Eq.5.13, i.e given by

$$G(p_t; \mu = p_{t,central}, \sigma_t) = \frac{1}{\sigma_t \sqrt{2\pi}} e^{-\frac{(p_t - \mu)^2}{2\sigma_t^2}}. \quad (5.14)$$

This could be easily done with the help of the implemented function of the ROOT class TRandom3, named *Gaus*, which generates a random number from the standard Gaussian distribution.

## 5.8 MC DECAY ROUTINE

In each loop out of  $N = 10^6$ , where N denotes the number of trials, the kinematic quantities were randomly generated, see Sec.5.6., for the  $D^{*+}$  resonance and the initial four-momentum was filled. The ROOT class TVirtualMCdecayer implements a void function *Decay*, which simulates the decay of the mother  $D^{*+}$  meson.

The information about both mother and daughter particles is then stored in an array of data, where the information contained in each entry corresponds to a certain particle. Then a loop over the entries of the array is programmed in order to identify each particle species. This identification is done by checking the PDG-code. Once a particle has been identified via its PDG-code, all necessary kinematic information is collected. The extracted parameters for

each particle were their energy  $E$ , transverse momentum  $p_t$ , pseudo-rapidity  $\eta$ , rapidity  $y$  and azimuth angle  $\phi$ . Each four-momentum of the particles was then filled as

$$P = \begin{pmatrix} E \\ p_t \cos \phi \\ p_t \sin \phi \\ p_t \sinh(\eta) \end{pmatrix}, \quad (5.15)$$

using the function *SetPtEtaPhiE* of the ROOT *TLorentzvector* class.

When the loop over all entries of the array was done, the next loop within the same decay of the mother D-resonance began, whereby the aim was to check the transverse momentum resolution and implement it into the simulation. Only particles with  $p_t \geq 100 \text{ MeV}/c$  could enter the new loop. A random value  $\tilde{p}_t$  was generated as  $\tilde{p}_t = \text{random.Gaus}(p_t, \sigma_{p_t})$  and another new four-momentum vector  $\tilde{P}$  was filled for each particle analog to the Eq.5.15., as the values of pseudo rapidity, azimuthal angle, as well as the z-component of the 3-momentum, were kept at their central values and the energy was calculated as  $\tilde{E} = \sqrt{m^2 + p_z^2 + \tilde{p}_t^2 \sinh^2(\eta)}$ , where  $m$  denotes the mass of the corresponding particle and  $p_z = p_t \sinh(\eta)$ .

The invariant masses  $\mathcal{M}_o$  and  $\mathcal{M}_*$  of  $D^o$  and  $D^{*+}$  and their difference  $\Delta\mathcal{M}$  were then calculated both with particle momentum resolution neglected (perfect detector) and included (realistic detector).

The corresponding four-momenta of charged detectable daughter particles were added together within each initial  $D^{*+}$  decay and then a function was added, implemented in *TLorentzvector* class, which extracted the invariant mass. It was calculated as follows

$$\mathcal{M}_o = (P_K + P_e) \rightarrow \mathcal{M}(); \quad (5.16)$$

$$\mathcal{M}_* = (P_K + P_e + P_\pi) \rightarrow \mathcal{M}(); \quad (5.17)$$

where  $P_K$ ,  $P_e$  and  $P_\pi$  denote the theoretical four-momenta of the kaon, positron and pion, respectively. The mass difference was then calculated as  $\Delta\mathcal{M} = \mathcal{M}_* - \mathcal{M}_o$ . The same procedure was used for the case of a realistic detector.

When each initial loop ended, the collected information, including the invariant masses, their difference, and all of the extracted and calculated kinematic quantities for each particle were saved into a block of data, called a *Tree* (elements of the ROOT class *TTree*). Each

physical quantity had its own *Branch* in the *Tree*. The data was then accessed and analyzed.

### 5.9 TRANSVERSE MOMENTUM DISTRIBUTIONS

The Fig. 5.5 displays the transverse momentum distributions of emitted pions within decay  $D^{*+} \rightarrow D^0\pi^+$ , as the value of transverse momentum of parent charged D-meson  $p_{t,D^{*+}}$  was kept at certain fixed value. The rapidity range of mother  $D^{*+}$  was  $|y| \leq 0.5$  for all cases and no kinematic selections were applied. For each distribution  $N = 10^5$  virtual decays were simulated with the help of MC-routine, see in Sec.5.8.

The Fig.pioni. depicts the distribution, as  $p_{t,D^{*+}} = 0$ , i.e. the D-resonance was assumed to be at rest in the laboratory frame. One can see, that the minimum transverse momentum value of pions is  $p_{t,\pi} = 0$ , i.e. the pion is emitted in beam-axis direction. The maximum of transverse momentum is reached when  $p_{t,\pi} = p = 38,4 \text{ MeV}/c$ , as  $p$  is the constant decay momentum. One can easily notice, that the number of pions with the threshold maximum transverse momentum is much more than the number of those, which fly in z-direction. Although, most of the emitted pions are boosted in beam direction, the distribution of polar angle  $\Theta$  is not uniform, as the polar angle denotes the angle between the transverse momentum and the whole momentum of the particle. Due to  $\Theta$ -distribution the transverse momentum profile has its specific shape.

The Fig.2-4 depict the transverse momentum distribution profiles of pions in the case, when the initial  $D^{*+}$ -resonance carries a non-zero value of transverse momentum. The minimum and maximum values of momentum, which pions can reach after the decay, are shown. These values agree with the theoretical predictions in Eq.4.10-4.11, see Sec.4.1. As the transverse momentum of  $D^{*+}$  increases, the boost in z-direction does not have a big impact on the direction of the 3-momentum of daughter particles. Because of the strong boost in transverse plane, more daughter pions fly in the orthogonal direction to the beam direction, i.e. the maximal polar angle gets smaller. Due to the reduction of the phase space, the distribution of transverse momentum becomes uniform in the case of large transverse momenta of mother D-meson.

The Fig.Ele. and Fig.Kaon show the transverse momenta distributions of positrons and kaons, respectively. As in the case of pions, no minimum bias selections were included and the kinematic cuts on transverse momentum of mother  $D^{*+}$  were the same. The minimum and maximum values that both positrons and kaons can reach agree with the theoretical predictions.

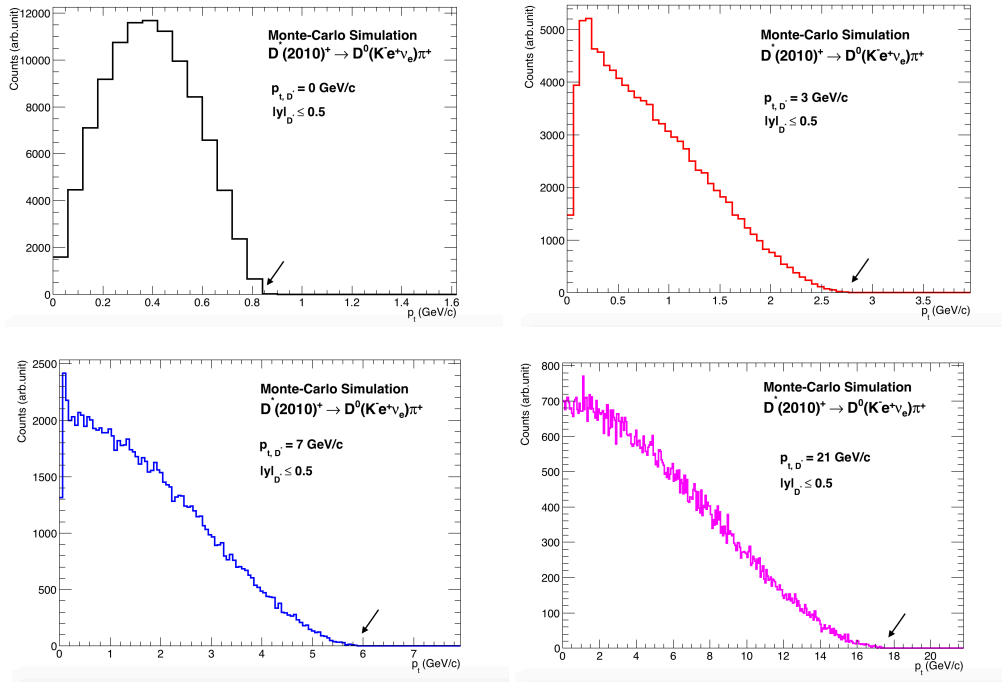


Figure 5.3: Transverse momentum distributions of positrons for different transverse momentum values of  $D^*$ . The arrows indicate the kinematic thresholds.

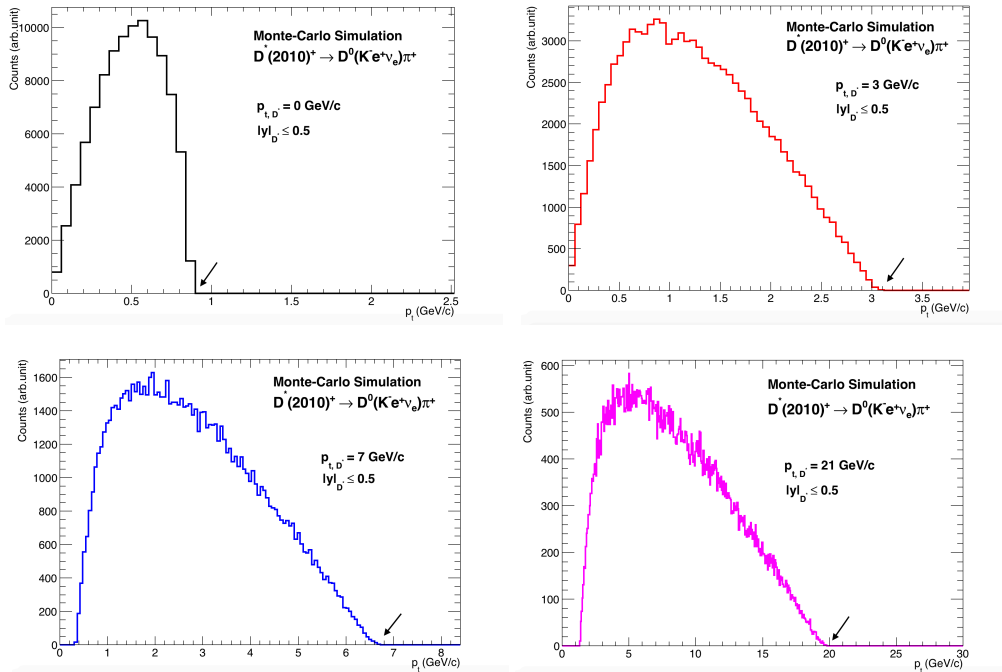
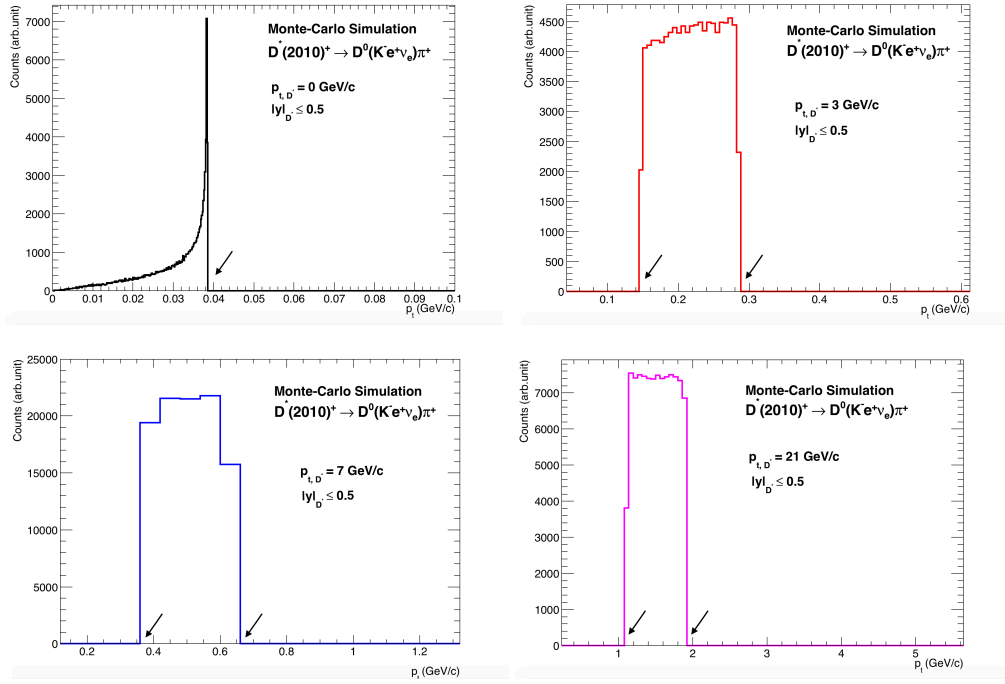


Figure 5.4: Transverse momentum distributions of kaons for different transverse momentum values of  $D^*$ . The arrows indicate the kinematic thresholds.



**Figure 5.5:** Transverse momentum distributions of pions for different transverse momentum values of  $D^*$ . The arrows indicate the kinematic thresholds.

As one can see, there are always positrons, whose 3-momentum is directed in the beam direction and that therefore do not reach the detector sensitive area. However, with the increasing transverse momentum of  $D^{*+}$  the number of positrons which do not pass the minimum bias trigger decrease.

The distribution of kaons  $p_t$  looks very similar to that of positrons, when the parent D-meson was at rest in the laboratory frame. However, the mean of the kaons distribution is shifted to the region of larger transverse momentum due to the kaons larger mass. One can notice, that in the case of both  $p_{t,D^{*+}} = 0$  and  $p_{t,D^{*+}} = 3$  there is a probability that kaons can be emitted in the beam direction. When the boost in transverse plane gets larger (Fig.3-4), all daughter kaons have a non-zero component of momentum in the transverse direction to the z-axis.

This effect is caused due to the relative large mass of kaons and could be predicted by Eq. which also predicts, that if for the transverse momentum of mother D-resonance holds  $p_{t,D^{*+}} \geq 4.6 \text{ GeV}/c$  than the daughter kaons, produced in  $D^{*+} \rightarrow D^0(K^- e^+ \nu_e)\pi^+$  can always be detected  $p_{t,K^-} \geq 100 \text{ MeV}/c$ , if one neglects the edge effects. On the other hand, the same equation predicts, that there always will be a non-zero probability that positrons can

be produced that do not reach detector at all, even if  $p_{t,D^{*+}} \geq 10^4 TeV/c!$  That implies that even in the case of usage of perfect detectors, i.e. neither spatial nor energy resolution, there always will be probability that not all of  $D^{*+}$ -candidates produced in the central collisions can be reconstructed in the decay channel, studied in this thesis.

Due to ITS+TPC good momentum resolution the simulated transverse momentum distributions for each charged daughter particle are with a good precision identical in shape, the detector resolution contributes insignificantly to the deviations in mean and width of the profiles.

### 5.10 RECONSTRUCTION OF INVARIANT MASSES

In order to reconstruct the invariant mass of a parent particle, one uses the information about detected daughter particles, such as the values of the energies and kinematic momenta, as the emitted particle interact with the matter in detectors. For instance, if a certain particle  $A$  decays into detectable particles  $B_1, B_2, \dots, B_n$  and if it is possible to collect data about all of those daughter particles within a given decay, then the invariant mass squared of the parent particle is simply the square of the sum of the reconstructed four momenta. For example, in the case of the decay  $D^{*+} \rightarrow D^0 \pi^+$  with the following "3-prong" (fully hadronic) decay of neutral D-meson  $D^0 \rightarrow K^- \pi^+$  all of the charged daughter particle are detectable. Therefore if the invariant mass is reconstructed neglecting any kinds of uncertainties, then one observes a Dirac delta distribution at mass point  $m = m_{D^0} = 2.01 \text{ GeV}/c$ . Fig 5.6 displays the reconstructed invariant mass of  $D^{*+}$ -resonance. The MC routine was the same as for analyses of the semi-leptonic decay  $D^{*+} \rightarrow D^0(K^- e^+ \nu^+) \pi^+$ . In particular the number of initial trials was assigned to be  $N = 10^6$  and the same resolution function was used as in Eq.5.13.

If one considers the detector resolution, broadening of the peak can be seen. However, the peak of the distribution shown in Fig.5.6 is still extremely narrow, i.e.  $\sim 50 \text{ KeV}$ , which can provide a good signal to background ratio and makes the signal detectable during the analyses of the collected experimental data.

The reconstruction of the masses  $M_0$  and  $M_*$  of  $D^0$  and  $D^*$ , respectively, in the decay chain  $D^* \rightarrow D^0(K^- e^+ \nu_e) \pi^+$  is more complex than e.g. in the "3-prong" decay of D-meson, since one of the daughter particles cannot be identified within detectors exploited at CERN - namely, neutrinos. As no real data about neutrinos can be collected, they must be excluded from the reconstruction routine. The mass of  $D^0$  is therefore obtained by analyzing the measured data only of kaons and positrons. In the case of  $D^*$ -meson, the only candidates are

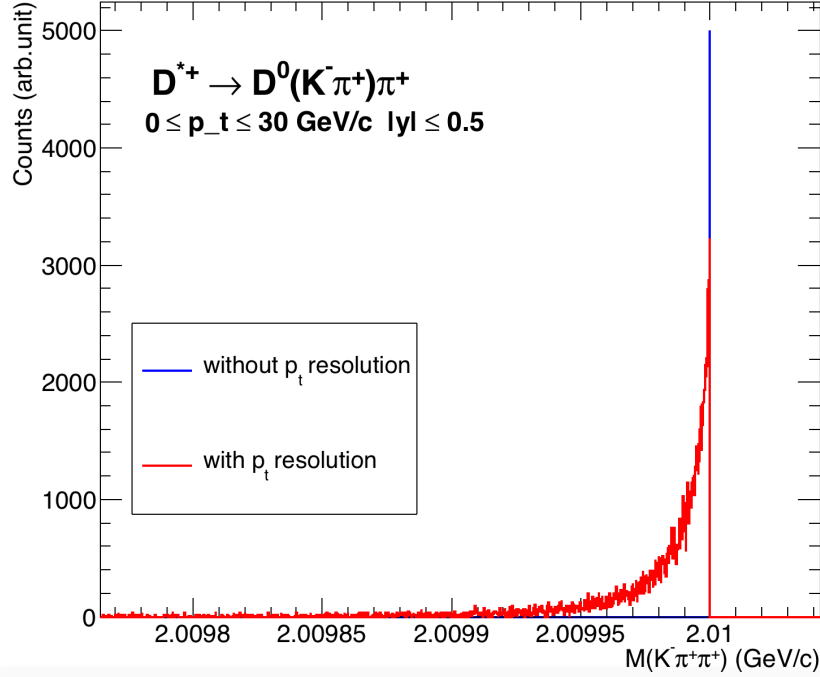


Figure 5.6: The reconstructed mass of  $D^{*+} \rightarrow D^0(K^-\pi^+)\pi^+$  without and with resolution

kaons, pions and positrons. Consequently, one does not expect a Dirac delta-distribution at the corresponding mass points  $m = m_{D^0}$  and  $m = m_{D^{*+}}$  in the case of ideal detector, as the undetectable neutrinos carry a fraction of the initial momentum of the parent particles. The invariant mass of the reconstructed  $D^0$  meson is calculated as

$$\mathcal{M}_0 = \sqrt{(P_{K^-} + P_{e^+})^2} \quad (5.18)$$

$$= \sqrt{m_{K^-}^2 + m_{e^+}^2 + 2(E_{K^-}E_{e^+} - \vec{p}_{K^-}\vec{p}_{e^+})}, \quad (5.19)$$

where the indices below the momenta, energies and masses define the species of the decay products. The calculation is analogous in the case of the  $D^{*+}$  meson, i.e  $\mathcal{M}_* = \sqrt{(P_{K^-} + P_{e^+} + P_{\pi^+})^2}$ . For brevity, the exact form of the expression will not be given here. The mass calculation is performed in the MC reconstruction routine, see Sec.5.8.

The calculated results are presented as plots of corresponding invariant mass distributions. The impact of the momentum resolution on the shape of the mass distributions is highlighted, as there are significant differences in the computed mass spectra when the resolution

is considered or neglected. Kinematic selections were applied on the analyzed data in order to consider abilities of detectors, i.e. only particles that fulfilled the following criteria were used in the mass reconstruction:

- 1) the kinematic threshold for both kaons and pions:  $p_T \geq 100 \text{ MeV}/c$
- 2) the rapidity range of each charged particle is the same as those of initial mother D-meson:  $-0.5 \leq y \leq 0.5$

Further distinction was made between minimum-bias conditions, i.e. positron transverse momentum of positrons  $p_t \geq 1 \text{ GeV}/c$ , and the data collection in online mode, i.e. with the trigger on positrons, leading to the kinematic selection  $p_t \geq 3 \text{ GeV}/c$ .

In order to retain clearer results, the transverse momentum of the initial  $D^*$ -meson was set to a certain value instead of observing the whole range from 0  $\text{GeV}/c$  to 30  $\text{GeV}/c$ . No changes were applied to the rapidity range.

#### 5.10.1 RECONSTRUCTION OF $\mathcal{M}_0$

The Fig.a-b displays the histograms of theoretically reconstructed invariant masses  $\mathcal{M}_0$  of the neutral  $D^0$ -meson. The momentum range of  $D^{*+}$  was  $0 \text{ GeV}/c \leq p_t \leq 30 \text{ GeV}/c$ , the kinematic selections were also included into both reconstruction routines. The invariant mass distribution in the Fig.a represents the case, when no transverse momentum resolution was regarded in the reconstruction routine. The distribution has its minimum at  $\mathcal{M}_{0,min} = m_K + m_e \approx 500 \text{ MeV}/c$ , which is equal to the sum of the kaon and positron masses, i.e. the minimum of  $\mathcal{M}_0$ -distribution is described by the case, when emitted neutrino takes the whole kinematic momentum of  $D^0$ -meson, thus leaving kaon and positron at rest in the laboratory frame. The maximum  $\mathcal{M}_{0,max} = \mathcal{M}_{0,theo} = 1.864 \text{ GeV}/c$  is reached, when neutrinos carry no kinematic energy in the laboratory frame at all, thus the whole energy of neutral D-meson is split between both detectable charged particles. One can easily notice, that both extreme kinematic cases are almost improbable. Furthermore, it is noticeable that since the invariant mass is Lorentz invariant, both minimum and maximum, as well as the shape, mean value and width of the theoretically predicted mass distribution will be independent of the kinematic of mother  $D^{*+}$ , as long as no kinematic selections are applied upon the charged daughter particles. However, those kinematic selections does not have a significant impact on the statistical parameters of mass distribution.

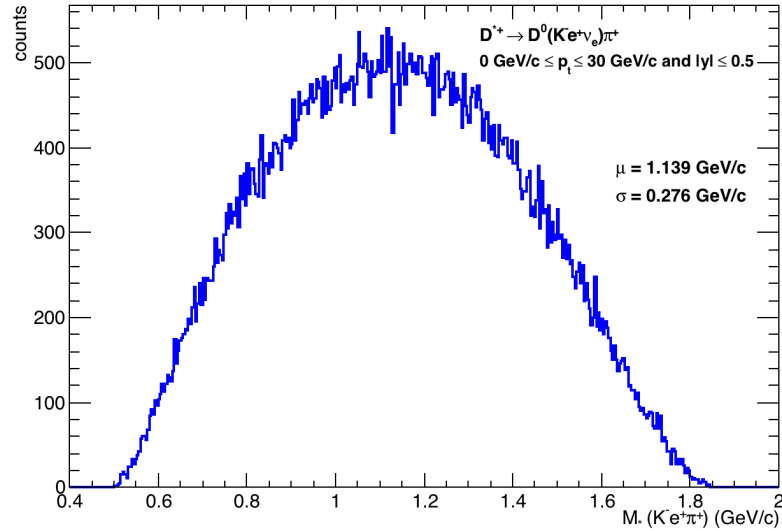


Figure 5.7: The reconstructed  $M_*$  without considering the momentum resolution

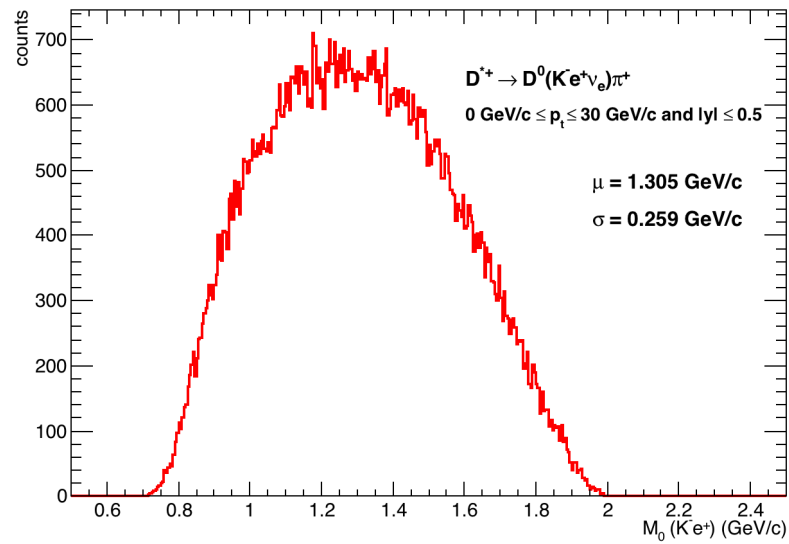
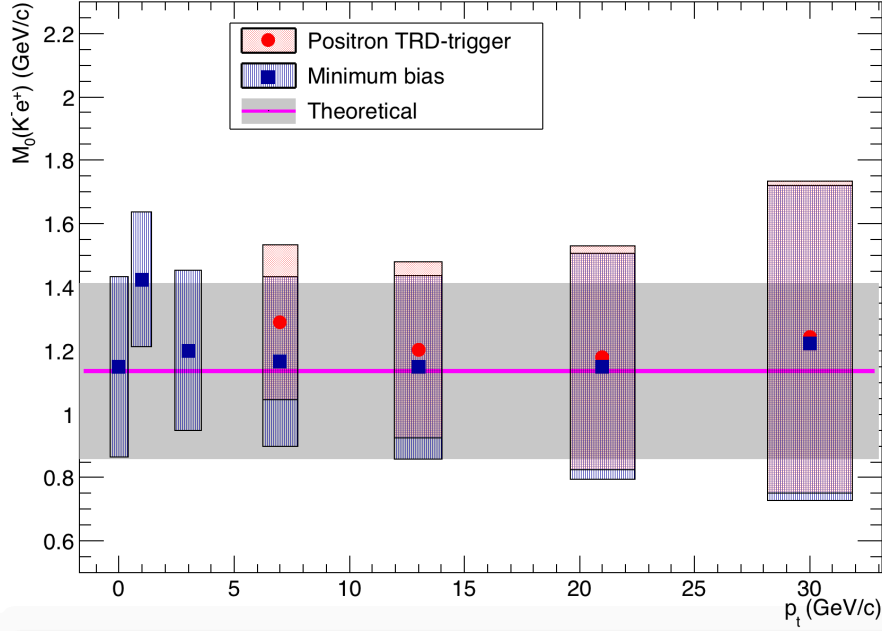


Figure 5.8: The reconstructed  $M_0$  without considering the momentum resolution



**Figure 5.9:** Invariant mass of  $D^0$  as a function of  $p_T$ . Pink line indicates mean value, shaded region corresponds to rms. The bars and circles (and small squares) indicate the rms of  $M_0$  distribution, when momentum resolution was taken into account

### 5.10.2 RECONSTRUCTION OF $M_*$

The data has been analyzed within the whole ranges of the transverse momentum,  $0 \leq p_{T,D^*} \leq 30 \text{ GeV}/c$ , and rapidity,  $|y| \leq 0.5$ . The data shown in fig(a) was collected from a simulation considering a *perfect* detector. In fig(b) the momentum resolution has been regarded (taken into account). The mean of the distribution in fig(a) is estimated to be *value<sub>mean</sub>* which lies under the theoretical value of the invariant mass  $m_{D^*} = 2.01 \text{ GeV}/c$ . The width of the peak is approximately  $\text{MeV}/c$ . If one takes momentum resolution into account, one sees the drastic broadening of the peak, the distribution is almost *value* times wider.

Fig.5.10 displays that high energy kaons and positrons contribute to the mass values of reconstructed  $D^0$  mesons larger than  $M_0 > 1.864$ . If one assumes that the measured transverse momenta of positron and kaon are  $\tilde{p}_{t,e} = p_{t,e} + n\sigma_e$  and  $\tilde{p}_{t,K} = p_{t,K} + m\sigma_K$ , respectively. Then one can estimate the variation of the  $M_0$  values (perfect detector).

$$\tilde{M}_0^2 \approx M_0^2 + 4(n\sigma_e + m\sigma_K)p_{t,e} \cdot p_{t,K} \sin\left(\frac{\Delta\phi}{2}\right)^2, \quad (5.20)$$

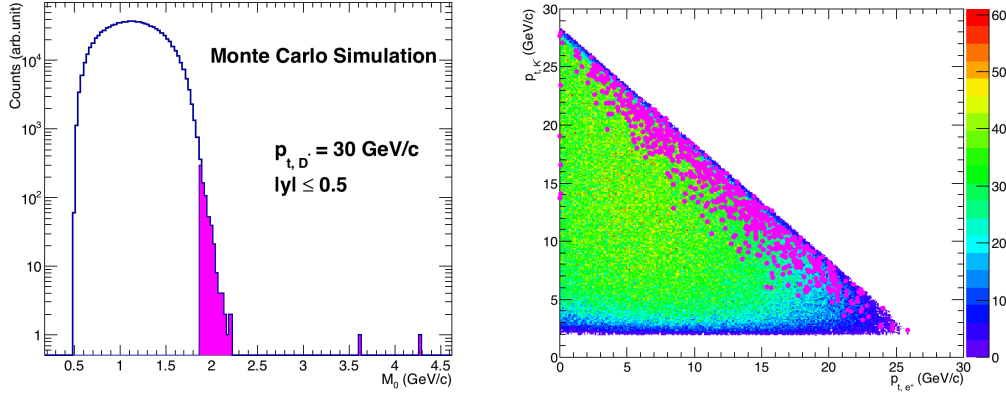


**Figure 5.10:** Left:  $M_0$  distribution for  $p_T = 30$  of  $D^*$  with considered momentum resolution. Right: positron transverse momentum vs. kaon transverse momentum. The magenta points on the right panel correspond to the magenta area on the left panel.

where  $\tilde{M}_0$  denotes the invariant mass of  $D^0$  obtained in MC simulation considering momentum resolution,  $\Delta\phi$  is the difference between the azimuthal angles of the emitted positron and kaon in the laboratory frame. The masses of the kaons and positrons are neglected in this calculation. For the momentum of kaon one should assume  $p_{t,K} \geq 10 \text{ GeV}/c$ .

### 5.10.3 DIFFERENCES OF INVARIANT MASSES

The invariant mass distributions of neutral D-meson and  $D^*$ -resonance seem to be very similar in shape and possess almost the same mean and width values. This similarity stems from the almost negligible energy contributions of emitted so called slow pions. In order to *visualize* the contributions from pions, momentum of  $D^0$ -mesons is plotted as a function of momentum of the parent D-meson, Fig.5.12. One easily notices a ray-like structure of the presented distribution. Together with the increasing momentum of parent D-meson the phase space of neutral daughter D-meson also gets larger. However, even at high value  $p_{T,D^*} = 30 \text{ GeV}/c$  the values of transverse momenta  $p_{T,D^0}$  can be found in a tiny range from roughly  $27 \text{ GeV}/c$  to  $28 \text{ GeV}/c$ . Moreover, one should compare the invariant masses of the examined D species, whose difference is  $m_{D^*} - m_{D^0} \approx 145 \text{ MeV}/c^2$ . It obviously implies that the emitted pion, whose mass is  $m_{\pi^+} \approx 140 \text{ MeV}/c^2$ , carries only very small fraction of the initial momentum.

The drawback of reconstructing the masses  $M_0$  and  $M_*$  separately lies mainly in the large width of the peaks. The contributions from combinatorial background, which is an inevitable part in the analyzes of real data, also have to be taken into account. Such broad peaks can be *lost* in this background and thus no information about the number of possible

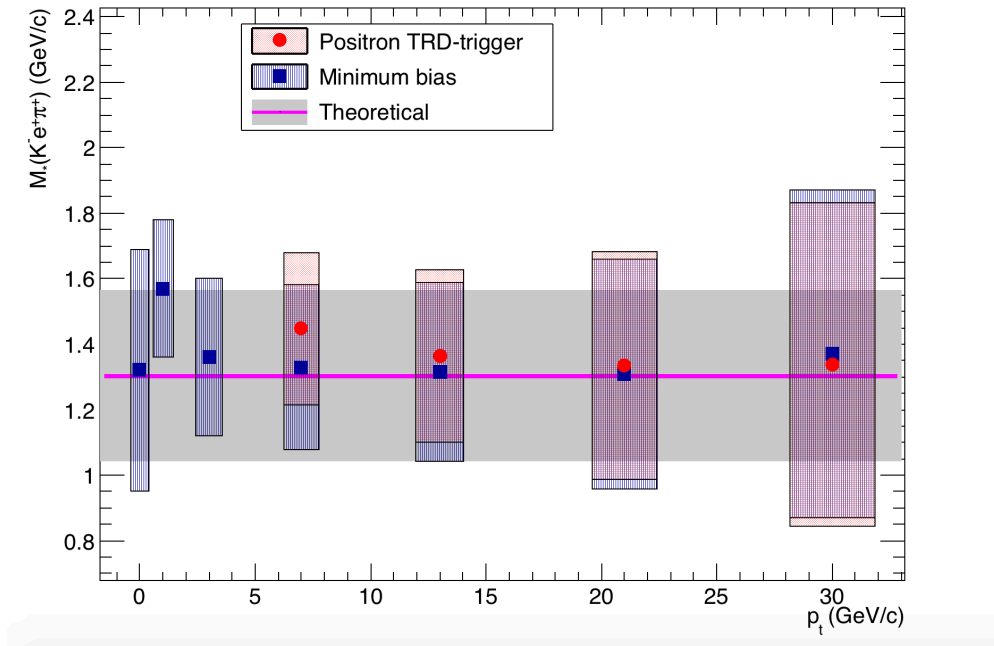


Figure 5.11: Invariant mass of  $D^*$  as a function of  $p_T$ . Pink line indicates mean value, shaded region corresponds to rms. The bars and circles (and small squares) indicate the rms of MO distribution, when momentum resolution was taken into account

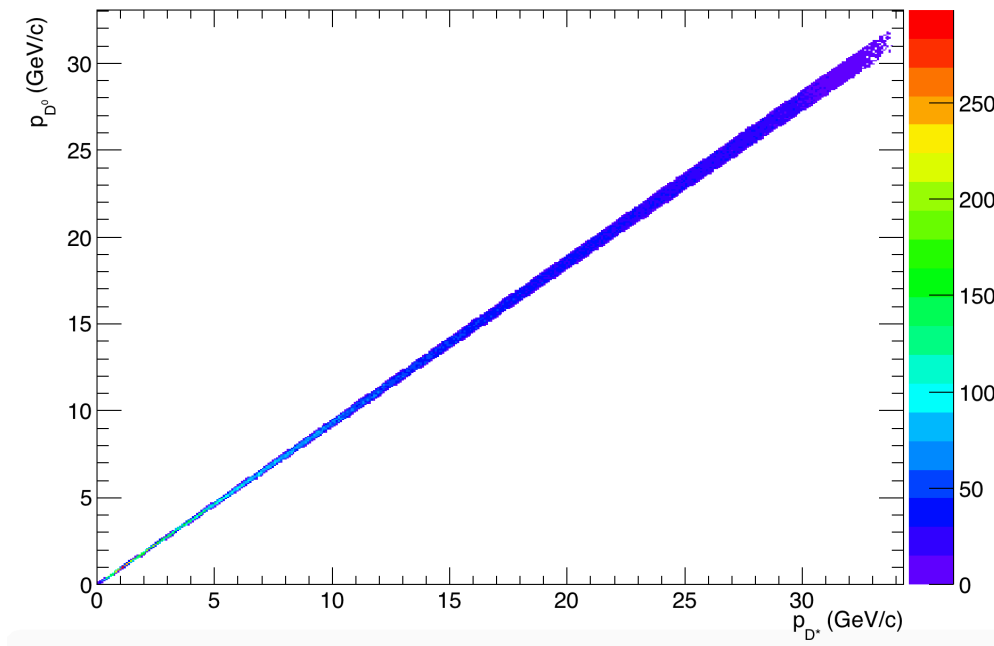


Figure 5.12: The whole momentum of  $D^0$  meson as function of the  $D^*$  momentum.

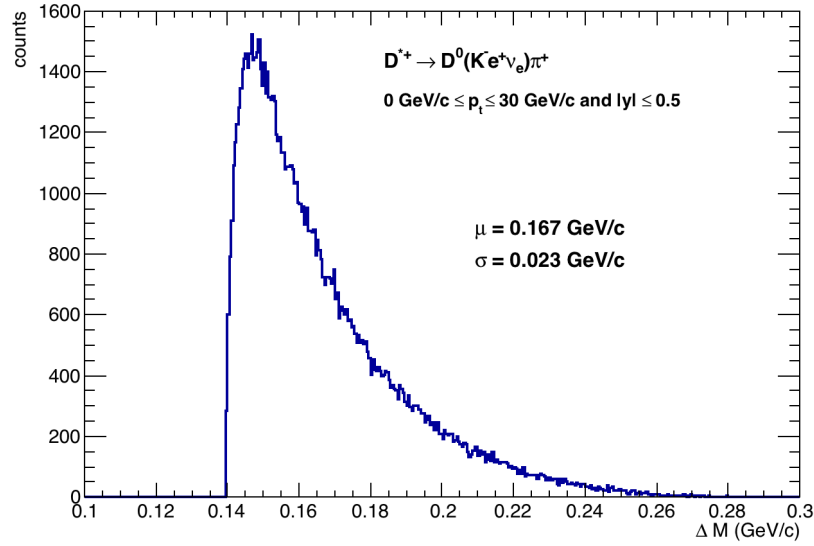
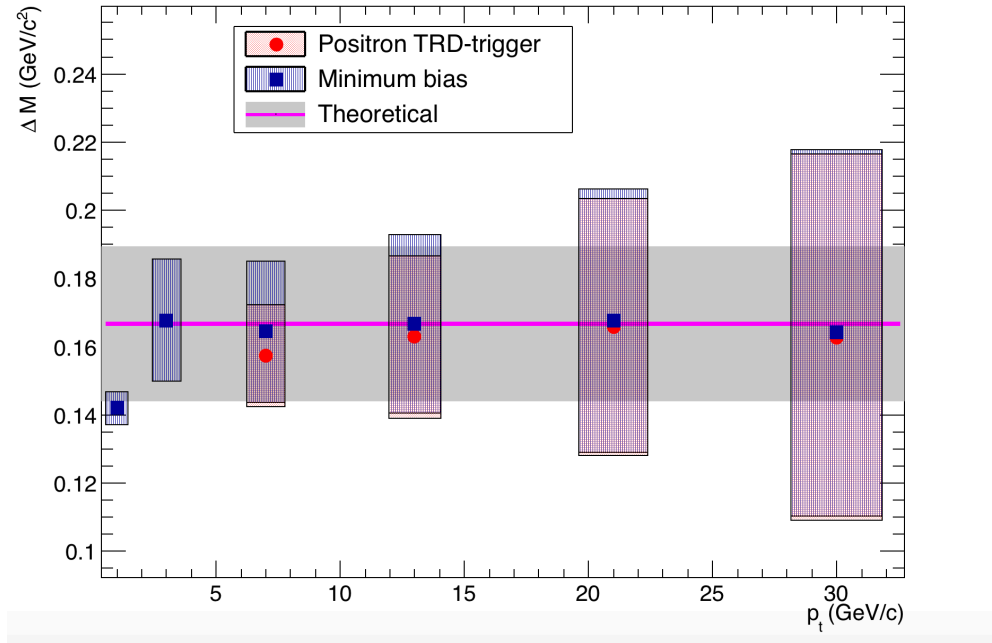


Figure 5.13: The reconstructed  $\mathcal{M}_*$  without resolution

$D^*$ -candidates can be executed. For this reason, the difference  $\Delta\mathcal{M} = \mathcal{M}_* - \mathcal{M}_0$  is calculated for the reconstructed invariant masses of D-mesons within each simulated decay chain. The plotted distributions of reconstructed  $\Delta\mathcal{M}$  are shown in *fig(c-ab)0-3opt, twodistributions*. The momentum and rapidity ranges are the same  $|y| \leq 0.5$ . Abrupt increase of the curve, *fig(ca)*, beginning at the invariant mass value of  $\Delta\mathcal{M} \approx m_{\pi^+} = 140\text{MeV}/c$  can be explained as the presence of kinematic threshold, i.e.theoretically, in the limit of vanishing kinematic momenta of all charged decay products the value of  $\Delta\mathcal{M}$  cannot be less than the invariant mass of the pion. The steepness of the increase might be explained by the *fact*(means) that most of the produced daughter kaons and positrons possess small values of the kinematic momentum. The slow tail of the distribution that reaches up to approximately  $260\text{MeV}/c^2$  appears as influence of presented neutrinos, which take fraction of energy,momentum with them.

It is also striking to take a closer look at  $\Delta\mathcal{M}$  distributions by the fixed values of transverse momentum of  $D^*$ . For this purpose, the decays have been simulated with the same Monte Carlo routine as before; however, this time  $p_{T,D^*} = n\text{ GeV}/c$  with  $n \in [0, 30]\text{ GeV}/c$ ,  $n \in \mathbb{N}$ . The number of trials have been chosen to be  $N = 10^6$  for each data generation routine. The Fig. below displays the results, as  $\Delta\mathcal{M}$  is plotted against the transverse momentum. All theoretically predicted  $\Delta\mathcal{M}$  distributions by each set value of  $p_{T,D^*}$  have had their mean at approximately  $\Delta\mathcal{M} = 0.167\text{MeV}/c$ , which is marked by the magenta horizontal line. The



**Figure 5.14:** Invariant mass difference  $\Delta M$  as a function of  $p_T$ . Pink line indicates mean value, shaded region corresponds to rms. The bars and circles (and small squares) indicate the rms of  $M_0$  distribution, when momentum resolution was taken into account

colorful band denotes the width of theoretical signals, simulated for distinct values of  $p_{T,D^*}$ . width can be found in a tiny interval from  $22,6 \text{ MeV}/c^2$  to  $22,7 \text{ MeV}/c^2$ .

A few values of the mean and the width of the peaks of  $\Delta M$  distribution with a considered momentum resolution are also displayed in the same graph. The peaks were simulated for certain values of  $p_{T,D^*}$ , namely, 1, 3, 7, 13, 21 and 30 GeV/c. One can see that TRD trigger does not allow the reconstruction of  $D^*$  candidates with a transverse momentum lower than 3 GeV/c. With the growing transverse momentum of the initial particle, the width of the peak is increases, since more charged daughter candidates obtain a larger transverse momentum. And the hit resolution worsens with increasing momentum.

#### 5.10.4 DETECTION EFFICIENCY

Detection efficiency, discussed in the following section, of a certain particle shows which fraction of the initial produced particles of this kind are detected. Of course, it is not realistic to expect, that efficiency reaches 100%. There are several reasons for this. First of all, the detector geometry yields to a certain data loss, i.e. finite size as well as incomplete space coverage

can lead to a direct particle loss. The granularity of the detecting medium can worsen track matching, thus reducing amount of data which could be analyzed. Secondary, there are certain kinematic thresholds *set on* particles. For example, charged particles with low momentum are bent on small radii in a magnetic field and therefore they do not even reach inner part of detectors. Furthermore, one should contemplate the trigger system, which selects only a fraction of the whole data.

The total efficiency  $\epsilon$  of reconstructed  $D^{*+}$  mesons is influenced by the contributions of geometric acceptance  $\alpha$  and positron efficiency  $\beta$ .

The geometric acceptance is calculated as a fraction of accepted  $D^{*+}$  candidates to the whole number of generated  $D^{*+}$  mesons. The parent particle counts to the accepted candidates, if emitted charged daughter particles reach the detectors. This implies that transverse momentum of all daughter candidates must be at least  $p_t \geq 100 \text{ MeV}/c$  and the corresponding rapidity might range between  $-0.5$  and  $0.5$  for each particle. The formula for  $\alpha$  is then given by

$$\alpha(p_T) = \frac{N_{D^{*+}}(s)}{N_{D^{*+}}}(p_T) \quad (5.21)$$

as  $s$  denotes the combination of all kinematic selections, listed above.

The positron efficiency is calculated as

$$\beta(p_T) = \frac{N_{D^{*+}}(s \cup p_{t,e^+})}{N_{D^{*+}}(s)}(p_T) \quad (5.22)$$

It means, that  $\beta$  is equal to the number ratio of those  $D^{*+}$  mesons, those daughter particles not only fulfill the selection criteria but also those daughter positrons survive in either the triggering system  $p_{t,e^+} \geq 3 \text{ GeV}/c$  or in the bias reconstruction  $p_{t,e^+} \geq 1 \text{ GeV}/c$ , to the accepted parent candidates. The total efficiency is then given by

$$\epsilon(p_T) = (\alpha \times \beta)(p_T) = \frac{N_{D^{*+}}(s \cup p_{t,e^+})}{N_{D^{*+}}}(p_T) \quad (5.23)$$

Each kind of efficiency ( $\epsilon$ ,  $\alpha$  and  $\beta$ ) is represented as a histogram over the transverse momentum of  $D^{*+}$ -meson,  $p_T$ . The range for the momentum is the same as *citewheretherangeisgiven*. Number of bins haven been chosen to be  $N = 30$ . This implies that i.e.  $N_{D^{*+}}(p_T)$  denotes the number of mother D-mesons collected in the momentum range  $(p_t + 0.5) \pm 0.5$  for  $p_t \in [0, 30] \text{ GeV}/c$ . The ratios have been calculated for each bin separately(respectively).The binomial error propagation has been applied to the calculated results. For example, the sta-

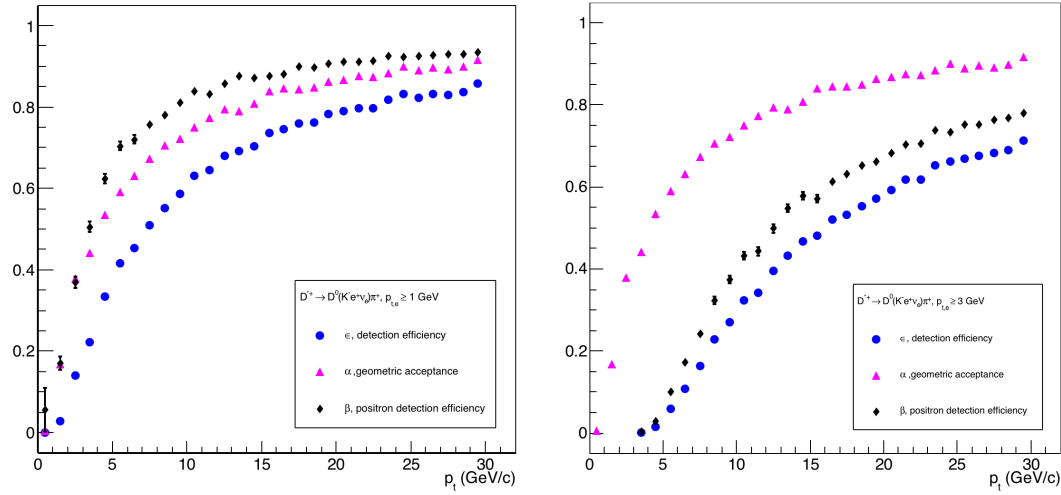


**Figure 5.15:** Geometrical acceptance, electron efficiency and total efficiency. On the left: the data has been analyzed in offline mode. On the right: the trigger on electrons has been applied

tistical error of the central value  $\epsilon(p_T)$  is then (?) calculated as

$$\Delta\epsilon(p_T) = \sqrt{\frac{\epsilon \cdot (1 - \epsilon)}{N_{D^{*+}}}}(p_T) \quad (5.24)$$

## 5.II EFFICIENCY RESULTS

The Fig.5.15. displays the efficiency functions. Due to the chosen big number of trials, the variance becomes very small for some of the entries and therefore is not visible almost over the whole momentum range. On the left picture in Fig.5.15. it has been assumed that positrons possessed a transverse momentum bigger or equal to  $1\text{GeV}/c$ . The picture on the right shows the results obtained for triggered positrons.

The total efficiency, as well as acceptance and positron efficiency, are very small at low values of momentum. Although, low momentum particles carry enough transverse momentum, in order to reach the detector material; due to possible high values of rapidity, i.e.  $|y| \geq 1$  not all of them come to the sensitive area of detectors. The rapidity of charged particles can reach values up to 1.5. For instance, in the case of  $p_T = 3\text{GeV}/c$  the percentage (the whole generated candidates) of pions, kaons and positrons in the measured rapidity range is 92% 75% and 60%, respectively. The increasing momenta lead to the enhancement of the efficiency, as the daughter particles are bent on a bigger radius and come to the detector. Moreover, due to large

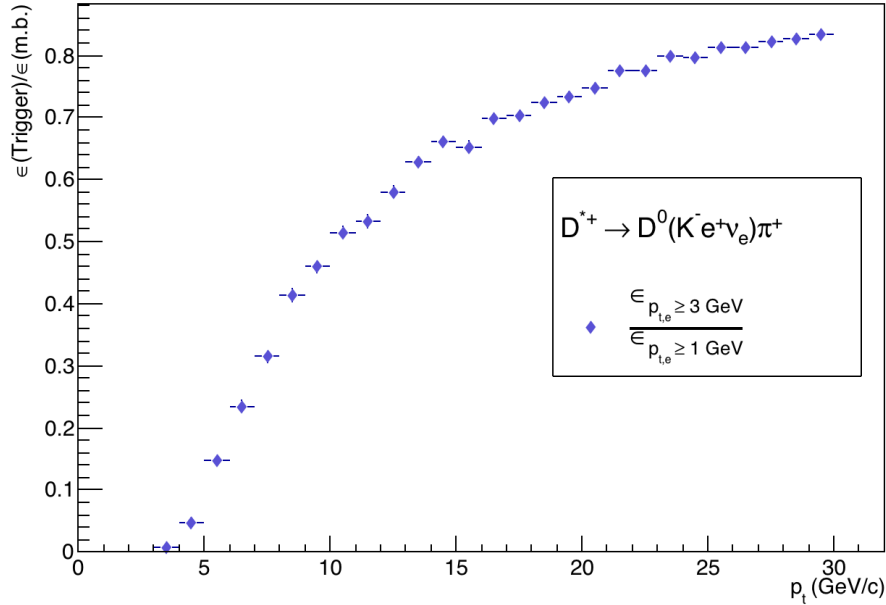


**Figure 5.16:** Fraction of the total detection efficiency considering TRD trigger to the efficiency considering minimum bias trigger

values of transverse momenta the boost in z-direction of the mother D-meson in the given rapidity interval does not have much impact on the rapidity ranges of the daughter particles. If  $p_{T,D^{*+}} = 30 \text{ GeV}/c$ , more than 95% of the daughter particles are found in the rapidity region  $|\gamma| \leq 0.5$ . The fluctuations of the entries (function, histogram) are connected to the statistical nature of the analyzed data. The acceptance  $\alpha$  is the same in the case for the both minimum bias and triggered events. The detection efficiency  $\epsilon$  of minimum bias data is much higher than those considering triggered positrons. Even at high momentum scales above  $20 \text{ GeV}/c$  it is probable to collect more than 20% of information(data). The ration of total efficiency functions is displayed in Fig.5.16

One sees on the right figure that almost no  $D^{*+}$ -meson with  $p_T \leq 5 \text{ GeV}/c$  can be detected. The mother D-mesons can be reconstructed with a probability of ca. 30%,if they have a high transverse momentum of about  $10 \text{ GeV}/c$ . This value of momentum will be selected as a threshold for following calculations. The enhancement of the efficiency  $\epsilon$  with increasing momentum implies that almost 70% of the generated mother particles survive the selection criteria and thus can be reconstructed.

# 6

## Number of particles

The number of predicted reconstructed  $D^{*+}$ -mesons is given as..

The differential number of  $D^{*+}$ -meson candidates, reconstructed in the semi-leptonic decay channel is given by

$$\left. \frac{dN_{D^*}}{dp_t} \right|_{|y| \leq 0.5} = A' \mathcal{L}_{int} \mathcal{B}(D^{*+} \rightarrow D^0(K^- e^+ \nu_e) \pi^+) \epsilon(p_t) \left. \frac{d\sigma^{FONLL}}{dp_t} \right|_{|y| \leq 0.5} \quad (6.1)$$

where  $A'$  denotes the product of nuclear modification factor  $R_{pA}$  and atomic mass number of the colliding nuclei  $A$  (see Sect.6.1),  $\mathcal{L}_{int}$  is the integrated luminosity (see Sect.6.2),  $\epsilon(p_t)$  is the total detection efficiency and  $\frac{d\sigma^{FONLL}}{dp_t}$  is a calculated differential cross section of charm hadron production with the help of FONLL software.  $\mathcal{B}(D^{*+} \rightarrow D^0(K^- e^+ \nu_e) \pi^+)$  is the branching ratio of the semi-leptonic decay and is calculated as

$$\mathcal{B}(D^{*+} \rightarrow D^0(K^- e^+ \nu_e) \pi^+) = \mathcal{B}(D^{*+} \rightarrow D^0 \pi^+) \cdot \mathcal{B}(D^0 \rightarrow K^- e^+ \nu_e) \approx 2.45\% \quad (6.2)$$

## 6.1 NUCLEAR MODIFICATION FACTOR

The nuclear modification factor  $R_{AA}$  is defined as

$$R_{AA} = \frac{d\sigma_{AA}/dp_t}{A^2 d\sigma_{pp}/dp_t}, \quad (6.3)$$

where the  $d\sigma_{AA}/dp_t$  and  $d\sigma_{pp}/dp_t$  denote the differential cross sections in Pb-Pb and p-p collisions, respectively., Völkl (2016). The atomic mass number is given by  $A = 208$  and stands for lead nuclei. If one assumes p-Pb collisions and keeps the value of the nuclear modification factor  $R_{AA} = R_{pA} \approx 1$ , then one can find the relation

$$\frac{d\sigma_{p-A}}{p_t} = R_{pA} A \frac{d\sigma_{pp}}{p_t} \approx 208 \cdot \frac{d\sigma_{pp}}{p_t} \quad (6.4)$$

## 6.2 LUMINOSITY AT ALICE

The luminosity  $\mathcal{L}$  is determined with the help of cross section measurement performed in the van der Meer scans. The luminosity of two colliding beams can be expressed by a relation

$$\mathcal{L} = \frac{N_1 N_2 f}{A_{eff}}, \quad (6.5)$$

as  $N_1$  and  $N_2$  denote the intensity of each beam,  $f$  stands for revolution frequency and  $A_{eff}$  is the effective interaction area in the transverse plane to the beam axis. The intensities of beams are determined experimentally and the revolution frequency is precisely known. The area  $A_{eff}$  is determined using the van der Meer method and e.g. in the case of two centrally colliding beams with a Gaussian density distribution  $\mathcal{L}$  is given by

$$\mathcal{L} = \frac{N_1 N_2 f N_b}{4\pi\sigma_x\sigma_y} \quad (6.6)$$

as  $\sigma_{x/y}$  depicts the beam width in the transverse plane and  $N_b$  is the number of bunches.

In the online mode the rate of p-p (or p-Pb, Pb-Pb) collisions  $R$  is measured and is related to cross section of event trigger as

$$R(t) = \sigma_{trigger} \mathcal{L}(t), \quad (6.7)$$

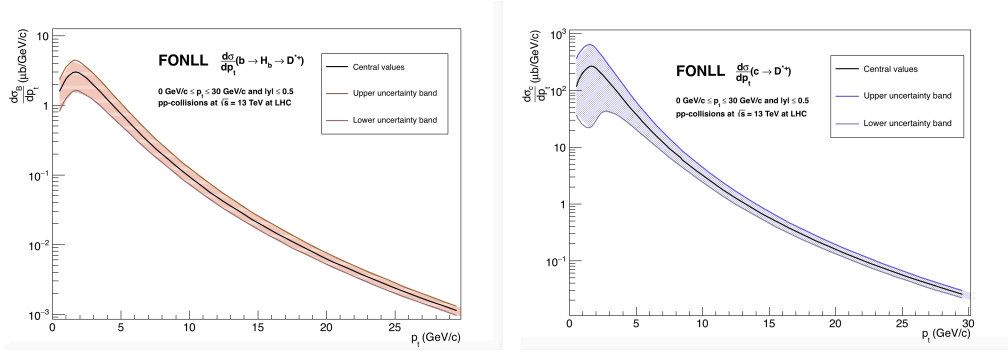


**Figure 6.1:** Left: Differential cross section of the prompt D hadron production calculated by the FONLL framework. Right: The differential cross section of D\* production from bottom quarks.

as  $\mathcal{L}(t)$  denotes the instant luminosity determined at certain time  $t$ . The number of particles  $N$  is then mathematically equal to the integration of the rate  $R(t)$  over the time of the measurement. Since the triggered cross section is assumed to be time independent, the relation can be found

$$N = \int R(t) dt = \sigma_{trigger} \int \mathcal{L}(t) dt = \sigma_{trigger} \mathcal{L}_{int}, \quad (6.8)$$

where  $\mathcal{L}_{int}$  denotes the integrated luminosity. The value of luminosity is then calculated as

$$\mathcal{L}_{int} = \frac{N}{\sigma_{trigger}}, \quad (6.9)$$

where the value of the cross section is  $\sigma_{trigger} = 2.22 \text{ b} \pm 0.01 \text{ b (stat)} \pm 0.06 \text{ b (syst)}$ , [ALICE collaboration \(2015\)](#), and  $N$  is the number of the detected events.

### 6.3 FONLL RESULTS

The fig1 and 2 display the differential cross sections  $d\sigma_c/dp_t$  and  $d\sigma_b/dp_t$  as functions of transverse momentum  $p_t$  for prompt  $c \rightarrow D^{*+}$  and "bottom" B feed-down  $b \rightarrow D^{*+}$  production, respectively. Both distributions were calculated assuming pp-collision,  $\sqrt{s} = 13 \text{ TeV}$  in the rapidity and transverse momentum ranges  $|y| \leq 0.5$  and  $p_t \in [0.5, 30.5]$ , respectively. The number of points was chosen to be  $n = 31$ . Moreover, the uncertainties of masses, scales and PDF's, which was set to CTEQ6.6, were regarded in both calculations. The branching ratio of D-resonance prompt production was equal to unity, i.e.  $f(c \rightarrow D^{*+}) = 1$ , and in the B feed-down  $f(b \rightarrow B \rightarrow D^{*+}) = 0.173$ , as  $B$  stands for an open-bottom hadron.

## 6.4 FEED-DOWN CORRECTIONS

The calculation of the cross section of B feed-down was performed, in order to estimate the feed-down contributions to the total open-charm hadron production.

The differential numbers of  $D^{*+}$ -candidates  $dN_c/dp_t$  and  $dN_b/dp_t$ , produced by the charm and bottom hadronization, respectively, are proportional to

$$\left. \frac{dN_{c,D^*}}{dp_t} \right|_{|y| \leq 0.5} = C_1 \left. \frac{d\sigma_c^{FONLL}}{dp_t} (c \rightarrow D^{*+}) \right|_{|y| \leq 0.5} \quad (6.10)$$

and

$$\left. \frac{dN_{b,D^*}}{dp_t} \right|_{|y| \leq 0.5} = C_2 \left. \frac{d\sigma_b^{FONLL}}{dp_t} (b \rightarrow B \rightarrow D^{*+}) \right|_{|y| \leq 0.5}, \quad (6.11)$$

as  $C_1$  and  $C_2$  represent the product of scaling and correction factors given in Eq.6.1. As one neglects topological selections and regard only kinematic selections and cuts, the total detection efficiency remains equal for both prompt and B feed-down D-meson production, and therefore  $C_1 = C_2$ . The total number of produced  $D^{*+}$ -mesons within heavy ion collisions is estimated as  $N = N_{c,D^*} + N_{b,D^*}$ . Therefore the differential fraction of the produced D-mesons by charm fragmentation is given as

$$\left. \frac{dN_{c,D^*}/dp_t}{dN/dp_t} \right|_{|y| \leq 0.5} = \frac{1}{1 + \left. \frac{d\sigma_b(b \rightarrow B \rightarrow D^*)/dp_t}{d\sigma_c(c \rightarrow D^*)/dp_t} \right|_{|y| \leq 0.5}} \quad (6.12)$$

The Fig.Correction depicts the differential fraction of Eq.6.12. For this purpose the calculated differential cross-sections  $d\sigma_c$  and  $d\sigma_b$  were, first of all, added up, i.e.  $d\sigma = f(c)d\sigma_c + f(b)d\sigma_b$ , regarding the scaling. The summation was performed for each entries of corresponding bins. Then the fraction was calculated. Considering that the charmed hadron production within the fragmentation of charm and bottom quarks is represented by uncorrelated processes, the total error was obtained by a Gaussian error propagation and is given explicitly as

$$\Delta \left( \frac{d\sigma_c}{d\sigma} \right) = \frac{1}{d\sigma} \sqrt{(d\sigma_c \Delta(d\sigma_b))^2 + (d\sigma_b \Delta(d\sigma_c))^2} \quad (6.13)$$

as  $d\sigma(b, c)$  stands for the number of entries in each corresponding  $p_t$ -bin. The error propagation was performed automatically by *Divide*-function of the histogram TH1D TClass for upper and lower uncertainty bands independently.

One can see that the differential fraction calculated for the central values is approximately

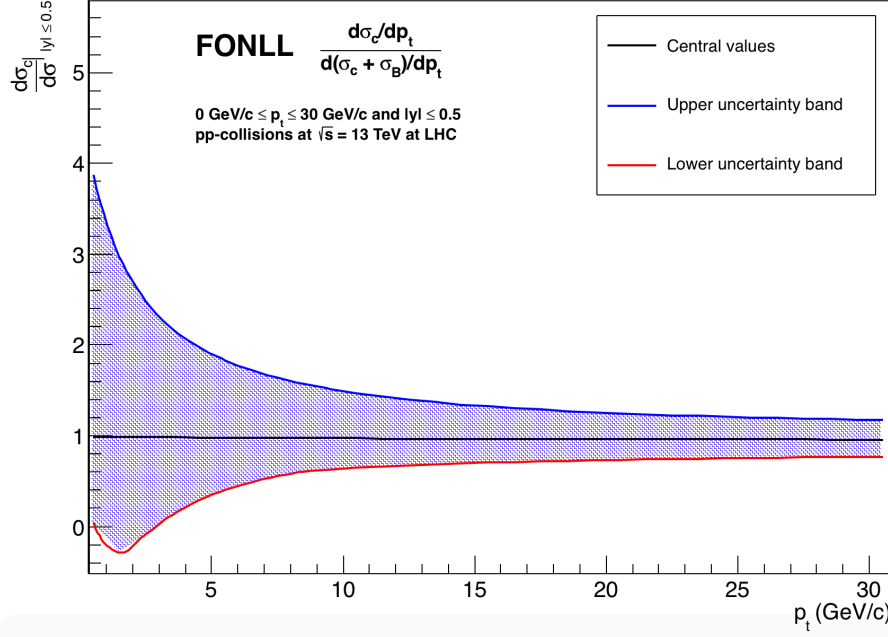


Figure 6.2: The fraction of the prompt  $D^*$  meson production to the total  $D^*$  meson production

equal to unity. The lower uncertainty band reduces the value of the differential fraction to approximately 0,85. We estimate the B feed-down correction to be 15%.

## 6.5 NUMBER OF RECONSTRUCTED PARTICLES

In order to calculate the theoretical predicted number of reconstructed  $D^{*+}$ -candidates in the p-Pb collisions, the differential cross section in Eq.6.1 must be integrated over the desired transverse momentum range, which is defined by the detection efficiency, which in turn is assumed to be more than 20%. When the offline analysis is done, i.e. the data was collected with the help of minimum bias trigger, the integration is performed in the range  $p_t \in [4, 30] \text{ GeV}/c$  and during the online analysis, i.e. the TRD-trigger filters the collection of data, the range  $p_t \in [8, 30] \text{ GeV}/c$ . One should also take into account the nuclear modification factor and the branching ratio of the decay channel. Since the values of corresponding luminosities (off-line, on-line data analysis) are dependent on the experiment, the numbers are given per luminosity

$$\frac{N_{MB,pPb}}{\mathcal{L}_{int}} = 2710_{20}^{+31} \quad (6.14)$$

and

$$\frac{N_{TRD-trigger,pPb}}{\mathcal{L}_{int}} = 322.7^{+2.04}_{-1.02} \quad (6.15)$$

# 7

## Data Analysis

The raw data, collected by ALICE in 2013 for pPb-collisions at  $\sqrt{s_{NN}} = 5.023 \text{ TeV}$ , was analyzed, in order to compare the theoretical predictions with the real processes. The analyzed data was collected during the online mode (TRD trigger) and included three periods LHC13d.pass4, LHC13e.pass4 and LHC13f.pass4. For this purpose the program, which was developed in AliROOT software and whose goal was to select good ESD-events, was supplemented by the additional loops over the selected ESD-events, in order to find the charged daughter particles for the following reconstruction of  $D^0$  and  $D^{*+}$  candidates. The reconstruction routine was as follows.

First of all, good ESD-events and ESD-tracks were selected by fulfilling certain kinematic and topological criteria. Then a loop over the tracks was performed. First loop was dedicated to identify positrons. The ESD-track corresponded to a positron, if the numbers of TOF and TPC sigmas  $n_{TOF}$  and  $n_{TPC}$  were found in the range  $-3 \leq n_{TOF}, n_{TPC} \leq 3$ . Moreover, the charge of the track had to be positive. When the positron was found, all needed kinematic information was extracted. The information extraction procedure was the same as in MC-simulation, however, that time the kinematic properties were obtained by functions, implemented in AliROOT class AliESDTrack. Then the next loop, i.e. the loop within

a loop, was built in, which was used to identify kaons by the same routine as for positrons. The ranges for TOF and TPC sigmas for kaon  $n_{TOF,K^-}$  and  $n_{TPC,K^-}$  were the same as in the case of positron identification. The charge of the ESD-track had to be negative. Once more the kinematic quantities were obtained. The last nest loop, a loop within kaon loop, over the ESD-tracks was used to identify pions. The charge of the track had to be positive and the constraints on the number of TOF and TPC sigmas of pions were again the same as for positrons and kaons. The extracted information for all charged daughter candidates included the values of all components of their 3-momentum  $p_x, p_y, p_z$  and the whole 3-momentum  $p$ , as well as values of energy  $E$  and rapidity  $y$ .

In the last nest loop, which used to identify pions, both the decay angles and the four-momenta for each charged candidate were constructed. For this purpose, a initialized element of the class `TLorentzvector` was filled with corresponding components of the 3-momentum and energy. The energy was found with the help of the function `GetEnergy(ESDtrack, m)`, as the `ESDtrack` denotes the currently analyzed good ESD-track and  $m$  stands for the theoretically predicted mass of the particle, which in turn was declared and defined manually in the program. Otherwise, if a certain particle could not be identified, its mass would be assumed to be equal to the mass of neutral pion  $m = 135 \text{ MeV}/c^2$ .

The masses of the  $D^0$  and  $D^{*+}$  candidates were found as

$$M_{o,ESD} = \sqrt{(P_{ESD,K^-} + P_{ESD,e^+})^2} \quad (7.1)$$

and

$$M_{*,ESD} = \sqrt{(P_{ESD,K^-} + P_{ESD,e^+} + P_{ESD,\pi^+})^2} \quad (7.2)$$

as well as, their difference  $\Delta M_{ESD} = M_{*,ESD} - M_{o,ESD}$  for each combination of charged daughter candidates. This implies, that if within a single positron loop exactly one positron, and in the nest loops  $n$  negative kaons and  $k$  positive pions were reconstructed, then the number of reconstructed  $D^*$  (and  $D^0$ ) candidates  $N$  was equal to  $N = n \cdot k$ . This calculation yielded a combinatorial background. The total number of events was  $N_{events} = 898228$ . The value of the integrated luminosity was then calculated to  $\mathcal{L}_{int} = 0.404 \mu\text{b}^{-1}$ , using Eq.6.9. The value in Eq.6.15 was then scaled with the determined value of luminosity, in order to estimate the number of the possible  $D^*$  candidates in the data sample.

The next step was to "filter" the combinatorial background. For this purpose we applied only kinematic selections on the data, i.e. the rapidity for each charged daughter candidate, as well as, for the reconstructed  $D^{*+}$ -candidates had to be in the desired range  $|y| \leq 0.5$ .

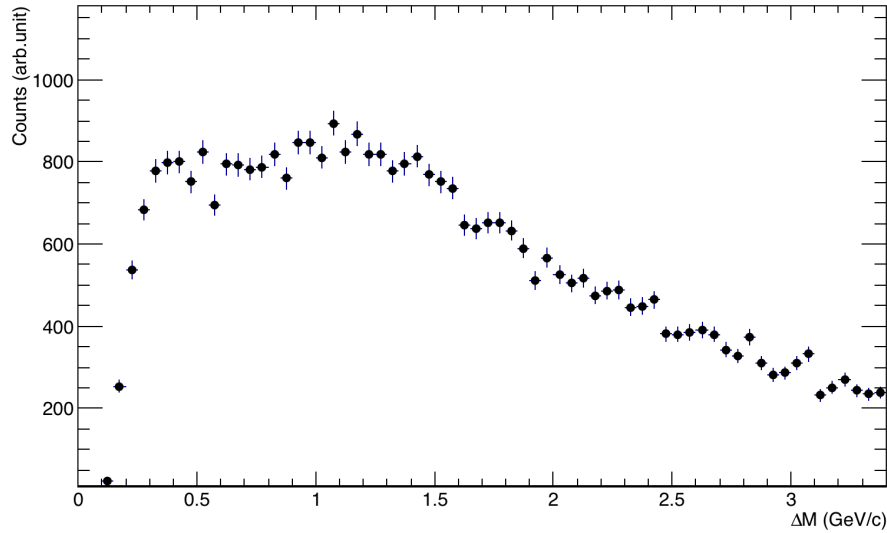


**Figure 7.1:** The  $\Delta M$  distribution. The analysis of the raw data.

Only those candidates were selected, which passed this selection. These selections reduced the number of possible  $D^*$  candidates to  $N_{selected} = 48238$ . However, one may observe, Fig. 7.1, that the combinatorial background was too high and no significant signal could be observed for the  $\Delta M$  distribution. This dramatically small signal to background ratio could be caused by the large number of pions, kaons and positrons which were produced the collisions.

The decay angle  $\Theta_\pi$  profile is shown for the selected pion candidates as the distribution of corresponding cosine functions in the cases of the theoretical predictions, i.e. obtained by MC-simulation, and during the reconstruction routine by the raw data analysis. One can observe, that as the MC-simulated  $\cos\Theta$ -distribution for pions are flat, the distribution of reconstructed candidates show the non-uniform behavior. It is noticeable, that most of the charged daughter particles are emitted either in the direction of reconstructed  $D^{*+}$  (and  $D^0$ ) candidates or in the opposite direction.

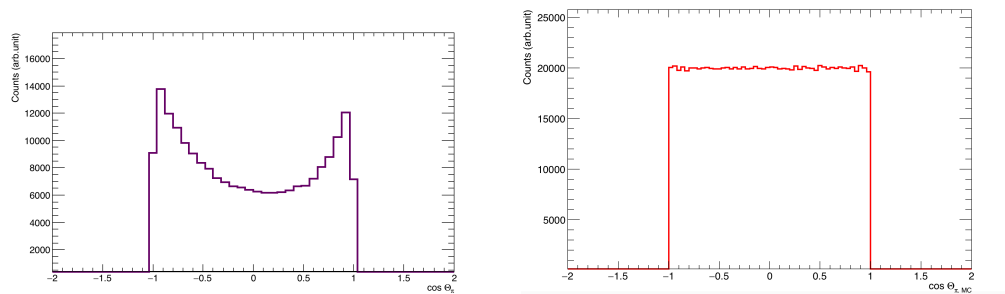


**Figure 7.2:** The distributions of the decay angle of the pion from  $D^{*} \rightarrow D^0$ . Left panel: the analysis of raw data. Right panel: MC simulation

# 8

## Summary

In this thesis the Monte-Carlo simulation was developed within the software ROOT using PYTHIA, in order to generate virtual decays of  $D^*(2010)^+$  in the semi-leptonic channel  $D^* \rightarrow D^0(K^- e^+ \nu_e)\pi^+$  using a flat rapidity distributions at mid-rapidity  $|y| \leq 0.5$  and transverse momentum  $p_t \in [0, 30] \text{ GeV}/c$  for the initial  $D^*$  resonance. An attempt was made at the theoretical prediction of the reconstruction efficiency of charmed D mesons in both the case of a minimum bias trigger and a TRD trigger in p-Pb collisions. An analysis of the influence of the transverse momentum resolution on the mass distributions was performed in this thesis.

The analyzed total detection efficiency, which considered only kinematic selections as the mid-rapidity ranges of charged daughter particles, minimum bias and TRD trigger requirements, has shown that only  $D^*(2010)^+$  candidates with  $p_t > 4 \text{ GeV}/c$  and  $p_t > 8 \text{ GeV}/c$  can be reconstructed with a better than 20% efficiency, if the charged daughter candidates fulfill the conditions of minimum bias and TRD triggers, respectively. Moreover, on the one hand the implemented trigger system forbids the reconstruction of very slow ( $p_t < 2 \text{ GeV}/c$ )  $D^*$ -mesons. On the other hand, a good positron detection efficiency enables very profitable reconstruction capabilities ( $> 60\%$ ) for  $D^*$ -mesons with  $p_t > 17 \text{ GeV}/c$ .

The  $\Delta\mathcal{M}$  reconstruction method was explicitly studied, with  $\Delta\mathcal{M} = M_* - M_o$ , where  $M_*$  and  $M_o$  are the reconstructed masses of mother D-resonance and the neutral  $D^o$ -meson, respectively. Due to the missing neutrinos from the decay  $D^o \rightarrow K^- e^+ \nu_e$  the independent reconstruction of both D-mesons, i.e.  $M_*$  and  $M_o$ , resulted in relatively broad signals with a width of about  $260 \text{ MeV}/c$  each, even in the case where  $p_t$ -resolution was not considered and it therefore appeared to be an ineffective method. However, the introduced  $\Delta\mathcal{M}$  method yielded a drastically enhanced narrow signal at a very clearly defined kinematic threshold equal to the pion mass, i.e.  $\Delta\mathcal{M}_{min} = 140 \text{ MeV}/c$  with a nearly ten times better resolution. The predicted theoretical value of the width of the  $\Delta\mathcal{M}$ -distribution was ca.  $23 \text{ MeV}/c$ . Due to the good relative transverse momentum resolution of the ITS+TPC, the  $\Delta\mathcal{M}$ -signal was found to be only up to 1.5% wider, even in the case of high-momentum daughter candidates, stemming from the decay  $D^*$  with  $p_t = 30 \text{ GeV}/c$ .

A calculation of the charm hadron production was performed with the help of the FONLL software for pp collisions at  $\sqrt{s} = 13 \text{ TeV}$ . These results helped to estimate a theoretically predicted a number of the  $D^{*+}$ -mesons produced within p-Pb collisions.

$$N_{D^*} \Big|_{pPb, \sqrt{s}=13 \text{ TeV}}^{TRD-trigger} = 132.9_{-0.51}^{+0.79}. \quad (8.1)$$

The developed reconstruction methods were applied on the raw data, stemming from LHC ALICE p-Pb collisions at  $\sqrt{s} = 5.02 \text{ TeV}/c$  from the year 2013 and selected by the TRD trigger system. The results clearly show that the application of only kinematic selections on the rapidity ranges of charged daughter candidates, as well as on the  $D^*$ -candidates, are not sufficient in order to get any valuable signal-to-background ratio. The high combinatorial background has its origin in the enormous amount of pions and kaons, whose relatively low masses lead to large production cross sections.

The extraction of the yield from raw data might be improved if other selective methods are regarded. Other kinematic selections included a selection on the expected invariant mass range, i.e.  $0.14 \leq \Delta\mathcal{M} \leq 0.2$ ; and the selection on the decay angle, i.e.  $-0.8 \leq \cos \Theta_\pi \leq 0.8$ , in order to reduce the number of charged candidates within jets. Moreover, topological cuts have to be taken into account. For instance, the inclusion of impact parameters, which

show the minimum distance between the track and the primary interaction vertex, are believed to be useful for an effective reconstruction of  $D^0$ -candidates.

The MC simulation can also be improved by considering other technical properties of ALICE detectors, among them e.g. the energy and spatial resolution provided by TPC and TRD. Furthermore, one should take into account the Bremsstrahlung of positrons.

# References

- Adronic, A. et al. (2016). *Eur.Phys.J. C76 107 arXiv:1506.03981*.
- Akindinov, A. (2010). The mrpc-based alice time-of-flight detector: Commissioning and first performance.
- ALICE collaboration (2010). Alignment of the alice inner tracking system with cosmic-ray tracks.
- ALICE collaboration (2014). Performance of the alice experiment at the cern lhc. *arXiv:1402.4476*.
- ALICE collaboration (2015). *arXiv:1405.1849*.
- Anticic,T. et al. (2005). The alice data-acquisition system. *IEEE Nuclear Science Symposium Conference Record*.
- Blum, L., Blum, M., & Shub, M. (1982). Advances in cryptology: Proceedings of crypto '82.
- Cacciari, M. et al. (1998). The p(t) spectrum in heavy-flavour hadroproduction. *arXiv:hep-ph/9803400*.
- Cakir, H. (2013). Precise determination of cc cross section in proton-proton collision at  $\sqrt{s} = 7$  tev. *Bachelor Thesis. University of Heidelberg*.
- Casella, G et al. (2004). Generalized accept-reject sampling schemes. *doi:10.1214/lnms/1196285403*.
- Dolgoshein, B. (1993). *Nuclear Instruments and Methods in Physics Research A326*.

- Garren, L., Knowles, I., Navas, S., Richardson, P., Sjostrand, T., & Trippe, T. (2016). *Monte Carlo particle numbering scheme*. <http://pdg.lbl.gov/2007/reviews/montecarlohpp.pdf>, [Online; accessed 19-Nov-2016].
- Glueckstern, R. (1963). Uncertainties in track momentum and direction, due to multiple scattering and measurement errors. *doi:10.1016/0029-554X(63)90347-1*.
- Hoermann, W. & Derflinger, G. (1990). *OR Spektrum (1990) 12: 181*. *doi:10.1007/BF01719718*.
- James, F. (1990). A review of pseudorandom number generators. *doi:10.1016/0010-4655(90)90032-V*.
- Klein, J. (2011). Triggering with the alice trd. *arXiv:1112.5110*.
- Lippmann, C. (2006). The alice transition radiation detector.
- Lippmann, C. (2012). *doi:10.1016/j.phpro.2012.02.390*.
- Lysovyyi, M., Verbytskyi, A., & Zenaiev, O. (2015). Combined analysis of charm-quark fragmentation-fraction measurements. *arXiv:1509.01061*.
- Mangano, Michelangelo L. et al. (1992). Heavy quark correlations in hadron collisions at next-to-leading order. *Nucl.Phys. B 373 (1992) 295-345*.
- Matsumoto, M. & Nishimura, T. (1998). Mersenne twister: a 623-dimensionally equidistributed uniform pseudo-random number generator. *ACM Transactions on Modeling and Computer Simulation. 8*.
- Moehler, C. (2014). D-meson production at ultra-low transverse momentum in proton-proton collisions with alice at the lhc. *Master Thesis*.
- Niebuhr, C. (2007). *Detectors in Elementary Particle Physics. Desy*.
- Olive, K.A. et al. (2014). *Chinese Physics C Vol. 38, No. 9 (2014) 090001*.
- Patrignani, C. (2016). *Passage of particles through matter*. <http://pdg.lbl.gov/2011/reviews/rpp2011-rev-passage-particles-matter.pdf>.
- Preghenella, R. (2009). The time-of-flight detector of alice at lhc: construction, test and commissioning with cosmic rays.

Skands, P.Z. (2015). Introduction to qcd. *arXiv:1207.2389v4*.

Sun, Y.I. et al. (2008). New prototype multi-gap resistive plate chambers with long strips. *arXiv:0805.2459*.

The CMS collaboration (2015). *CMS PAS HIN-15-012*.

The OPAL Collaboration (1997). *arXiv:hep-ex/9708021*.

Völkl, M. (2016). *PhD Thesis*.

# Acknowledgments

THE SUCCESSFUL PREPARATION of this thesis was possible only with much help and continuous support from many friends and colleagues.

I sincerely thank my supervisor Dr. Kai Schweda for his support and ever caring nature throughout the course of my bachelor thesis. I am indebted to Dr. Yvonne Pachmayer for her help with raw data analysis and providing me with valuable advise whenever she got a chance..

I am also very grateful to Dr. Jeremy Wilkinson, who helped me with proofreading and with the FONLL. A special thank you to Alex Golovin for taking the time out to review and proofread my thesis.

They are some of the nicest and most helpful people that I have come across.

# Erklärung

Hiermit versichere ich, dass ich die vorliegende Arbeit selbstständig verfasst und keine anderen als die angegebenen Quellen und Hilfsmittel benutzt habe, dass alle Stellen der Arbeit, die wörtlich oder sinngemäß aus anderen Quellen übernommen wurden, als solche kenntlich gemacht und dass die Arbeit in gleicher oder ähnlicher Form noch keiner Prüfungsbehörde vorgelegt wurde.

Heidelberg, den December 12, 2016